Entanglement scaling behaviors of free fermions on hyperbolic lattices

Xiang-You Huang,[1,*] Yao Zhou,[1,2,*] and Peng Ye[1,†]

[1]Guangdong Provincial Key Laboratory of Magnetoelectric Physics and Devices, State Key Laboratory of Optoelectronic Materials and Technologies, and School of Physics, Sun Yat-sen University, Guangzhou 510275, China

[2]Department of Physics, The University of Hong Kong, Pokfulam Road, Hong Kong SAR, China

(Received 21 August 2024; accepted 7 April 2025; published 29 April 2025)

Recently, tight-binding models on hyperbolic lattices (discretized anti–de Sitter space) have gained significant attention, leading to hyperbolic band theory and non-Abelian Bloch states. In this paper, we investigate these quantum systems from the perspective of quantum information, focusing particularly on the scaling of entanglement entropy (EE) that has been regarded as a powerful quantum-information probe into exotic phases of matter. It is known that on a d-dimensional translation-invariant Euclidean lattice, the EE of band insulators scales as an area law ($\sim L^{d-1}$, where L is the linear size of the boundary between two subsystems). Meanwhile, the EE of metals [with a finite density of state (DOS)] scales as the renowned Gioev-Klich-Widom scaling law ($\sim L^{d-1}\ln L$). The appearance of logarithmic divergence, as well as the analytic form of the coefficient c, is mathematically controlled by the Widom conjecture of asymptotic behavior of Toeplitz matrices and can be physically understood via the Swingle's argument. However, the hyperbolic lattice, which generalizes translational symmetry, results in the inapplicability of these analytic approaches and the potential nontrivial behavior of the EE. Here we make an initial attempt through numerical simulation. Remarkably, we find that both cases adhere to the area law, indicating the effect of background hyperbolic geometry that influences quantum entanglement. To achieve the results, we first apply the vertex-inflation method to generate a hyperbolic lattice on the Poincaré disk, and then apply the Haydock recursion method to compute the DOS. Finally, we study the scaling of the EE for different bipartitions via exact diagonalization and perform finite-size scaling. We also investigate how the coefficient of the area law is correlated to the bulk gap in the gapped case and to the DOS in the gapless case, respectively. Future directions are discussed.

DOI: 10.1103/PhysRevResearch.7.023098

I. INTRODUCTION

Quantum-information theory provides a novel approach to study nonlocal correlations of quantum many-body systems [1–3]. To quantify these nonlocal correlations, the celebrated entanglement entropy (EE), or von Neumann entropy, plays an important role and exhibits universal features. For instance, the scaling behavior of the EE reveals the underlying nature of the systems [1–8]. In systems with an energy gap, the leading term of the EE for ground states satisfies the area law $S_A \sim L_A^{d-1}$ [2,3,6], where d is the spatial dimension and L_A is the linear size of the boundary between two complementary subsystems denoted as A and B. For gapless systems, conformal field theory (CFT) provides an insight into the scaling of the EE in one-dimensional (1D) gapless systems [9,10]. Furthermore, for higher-dimensional free-fermion systems with a codimension-1 Fermi surface, the application of the Widom conjecture [11] gives the scaling of the leading term of the EE, which leads to the Gioev-Klich-Widom scaling (also dubbed "super-area law") $S_A \sim L_A^{d-1}\ln L_A$ [12,13]. Meanwhile, Swingle proposed a simple reconstruction method to physically understand the origin of the logarithmic divergence term and the analytic form of the coefficient c [14]. The logarithmic divergence, to some extent, indicates that the presence of an infinite number of gapless fermion modes significantly enhances entanglement.

It is worth noting that these scaling behaviors are established on the translation-invariant lattices with Euclidean geometry, where the Widom conjecture of asymptotic behavior of Toeplitz matrices is applicable. Therefore, we raise the question of whether the behaviors of the EE could be significantly changed by the background geometry, as we find that entanglement on a fractal lattice can exhibit a fractal-like distribution and generalized area law reflecting the boundary Hausdorff dimension [15]. In fact, non-Euclidean geometry is prevalent in natural and artificial systems [16]. Anti–de Sitter (AdS) space, characterized by negative spatial curvature, is widely studied in various fields of physics [17–25]. The hyperbolic lattice, which can be viewed as a discretization of AdS space, is of interest in high-energy physics [26–29]. Recently, hyperbolic lattices have been experimentally simulated on many platforms [30–35] and have drawn more and more attentions in various fields of condensed matter

*These authors contributed equally to this work.
†Contact author: yepeng5@mail.sysu.edu.cn

TABLE I. Scaling behavior of the EE of ground states of free-fermionic systems on a *d-dimensional* Euclidean lattice with translation invariance, fractal lattice with self-similarity, and *two-dimensional* hyperbolic lattice. In the fractal case, d_{bf} denotes the *Hausdorff dimension* of the boundary of subsystem A, while the EE of gapless systems exhibits a fractal-like distribution [15].

Lattice	Phase	S_A
Euclidean lattice [2,3]	Gapped, DOS $= 0$	$\sim L_A^{d-1}$
	Gapless, DOS > 0	$\sim L_A^{d-1} \ln L_A$
Fractal lattice [15]	Gapped, DOS $= 0$	$\sim L_A^{d_{\mathrm{bf}}}$
	Gapless, DOS > 0	$\sim L_A^{d-1} \ln L_A$
Hyperbolic lattice	Gapped, DOS $= 0$	$\sim L_A$
	Gapless, DOS > 0	$\sim L_A$

physics [36–53]. The hyperbolic lattice is very different from its Euclidean counterpart due to its non-Abelian translation symmetry [54–57]. Remarkably, these geometric properties lead to the hyperbolic band theory (HBT) for tight-binding models on hyperbolic lattices [55–59].

The absence of Euclidean translation invariance on a hyperbolic lattice results in the inapplicability of the Widom conjecture of Toeplitz matrices, implying that the EE may exhibit nontrivial behaviors. Motivated by the rapid progress on hyperbolic lattices as well as the application of quantum information in many-body physics, in this paper we explore the potential role of hyperbolic geometry in affecting quantum entanglement. However, the analytic difficulties are significantly challenging as the Widom conjecture of Toeplitz matrices is no longer applicable. Therefore, our goal is to provide numerical evidence of the exotic interplay of quantum entanglement and hyperbolic geometry by investigating the scaling of the EE of free-fermion systems on hyperbolic lattices. We observe that for gapped systems, the EE still scales as the area law, consistent with our expectations on a Euclidean lattice. However, for gapless system with finite DOS, we discover that the super-area law breaks down and the EE adheres to the area law instead. This area-law scaling reflects the nontrivial effect of hyperbolic geometry for entanglement, which may relate to a holographic understanding that could be experimentally studied [19,34]. Moreover, similar to our previous work in fractal geometry as summarized in Table I, our results suggest a perspective to study the geometry of quantum systems through entanglement.

To achieve our research objectives, our methodology begins with the application of the vertex-inflation method [48,60,61]. This method is instrumental in creating a hyperbolic lattice configuration on the Poincaré disk, which serves as the foundational structure for our computational study. Following the lattice creation, we employ the Haydock recursion method [62–65] to compute the DOS within this hyperbolic framework. This computational technique is well suited for handling the complex geometries inherent in hyperbolic lattices, providing a detailed characterization of electronic states and their distribution [62]. Subsequently, we proceed to obtain the eigenspectrum of nonsparse reduced density matrices via exact diagonalization and various kinds of bipartitions between the two subsystems. To obtain the scaling behaviors, we perform finite-size scaling analyses, which enables us to extrapolate our findings across different subsystem sizes, revealing how entanglement quantities scale with the boundary of the subsystem. Furthermore, a central aspect of our investigation involves exploring correlations between the coefficient of the area law, bulk gap, and DOS. As hyperbolic lattices can be experimentally realized through various techniques, it will be interesting to experimentally measure entanglement on hyperbolic lattices via, e.g., a phononic platform [66]. Interestingly, the area law of both gapless and gapped systems implies that the matrix product states (MPS) and projected entangled-pair states (PEPS) [25,67,68] may be potentially efficient in simulating quantum spin liquids with gapless spinons with finite DOS on a hyperbolic lattice.

This paper is arranged as follows: In Sec. II, we specify the construction of hyperbolic lattices and provide a brief summary of studying free-fermion entanglement entropy. Next, in Sec. III, we study the EE of gapless free-fermion systems with finite DOS and the dependence of the scaling coefficient on DOS, while in Sec. IV, we study the EE of gapped free fermions on hyperbolic lattices. Finally, we summarize our findings in Sec. V and discuss their potential applications. Additionally, we detail the hyperbolic lattice setup and discuss the volume law in Appendix A, provide supplemental data of the EE in Appendix B, and review the approach to compute the DOS in Appendix C. We provide the finite-size scaling analysis in Appendix D and the analysis of super-area law in Appendix E. We discuss the asymptotic behavior of the coefficient of the area law in Appendix F.

II. PRELIMINARIES

A. Tessellations of plane

In the beginning, we introduce the tessellations (or tilings) of the Euclidean and hyperbolic plane. A two-dimensional plane can be tessellated by regular polygons, denoted by the Schläfli symbol $\{p, q\}$ [54], where the integers p and q represent that the plane is tessellated by regular p-edge polygons, with each lattice site having coordination number q. For instance, as demonstrated in Fig. 1(a), each square has edges $p = 4$ and each lattice site has coordination number $q = 4$ for square lattice $\{4, 4\}$. For the two-dimensional plane with Euclidean geometry, p, q should satisfy the constraint $(p-2)(q-2) = 4$, which means that there are only three possible tessellations, including the triangular lattice $\{3, 6\}$, the square lattice $\{4, 4\}$, and the hexagonal lattice $\{6, 3\}$. In addition, when p and q satisfy $(p-2)(q-2) > 4$, these tessellations can be adopted to discretize the hyperbolic plane and Fig. 1(b) demonstrates a $\{4, 6\}$ lattice.

Before constructing hyperbolic lattices, we need to specify the coordinates under which we are handling our studies. To assign a complex coordinate to each lattice site, we employ a conformal disk model of hyperbolic space, i.e., Poincaré disk, as shown in the right-hand side of Fig. 1(c). By using this conformal map, the lattice is embedded in a unit disk $\mathbb{D} = \{z \in \mathbb{C}, |z| < 1\}$ with metric

$$ds^2 = (2\kappa)^2 \frac{|dz|^2}{(1-|z|^2)^2}, \tag{1}$$

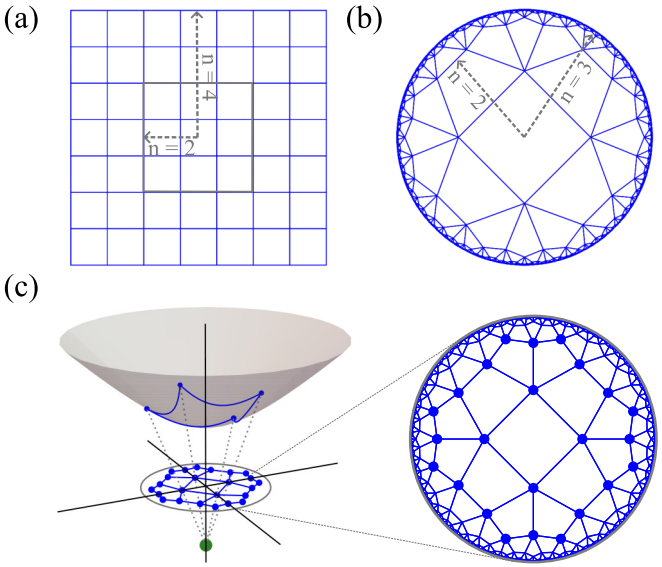

FIG. 1. Tessellations of a two-dimensional plane and projection of hyperbolic lattice. (a) Euclidean $\{4, 4\}$ lattice. (b) Hyperbolic $\{4, 6\}$ lattice. The gray labeled dashed line denotes the order n of the ring. (c) Projection of a $\{4, 6\}$ lattice onto a Poincaré disk. A site on the hyperboloid $\hat{z}^2 - \hat{x}^2 - \hat{y}^2 = 1$ is projected onto a unit disk on the $\hat{z} = 0$ plane by intersecting it with a line drawn through $(0, 0, -1)$.

where κ is the constant radius curvature and its corresponding constant curvature is $K = -\kappa^{-2}$. From Eq. (1), the geodesic distance σ between two sites z and z' on the Poincaré disk is given by

$$\sigma(z, z') = \kappa \operatorname{arcosh}\left(1 + \frac{2|z - z'|^2}{(1 - |z|^2)(1 - |z'|^2)}\right), \quad (2)$$

where z denotes a site on the disk with complex coordinate $z = x + \mathrm{i}y = re^{\mathrm{i}\phi}$.

B. Hyperbolic lattice construction and the exponential wall

Next, we consider using the regular tilings to generate hyperbolic lattices. By adopting the vertex-inflation method (or vertex-inflation tiling procedure) [48,60,61], we can effectively generate Euclidean and hyperbolic lattices of various rings where the sites are located. To obtain a finite $\{p, q\}$ lattice, we initially generate a regular p-edge polygon at the center of the Poincaré disk, labeled as the first ring, and then attach new rings to it iteratively. In Fig. 2, we show the generating procedure of a $\{4, 5\}$ lattice, where the bold sites denote the outermost ring that was generated in each iterative step. By repeating this process, we can successively enlarge the size of the lattice based on the outermost ring, allowing us to obtain an arbitrarily large lattice with any number of rings. More detailed information on this procedure can be found in Appendix A.

In the following, we use $\{p, q, n\}$ rather than $\{p, q\}$ to label a concrete finite hyperbolic lattice, i.e., flake, for numerical computations, where the integer n represents the number of rings included in the lattice, as shown in Figs. 1(a) and 1(b) by the dashed line. An important feature of a hyperbolic lattice is that the total number of lattice sites, N, increases

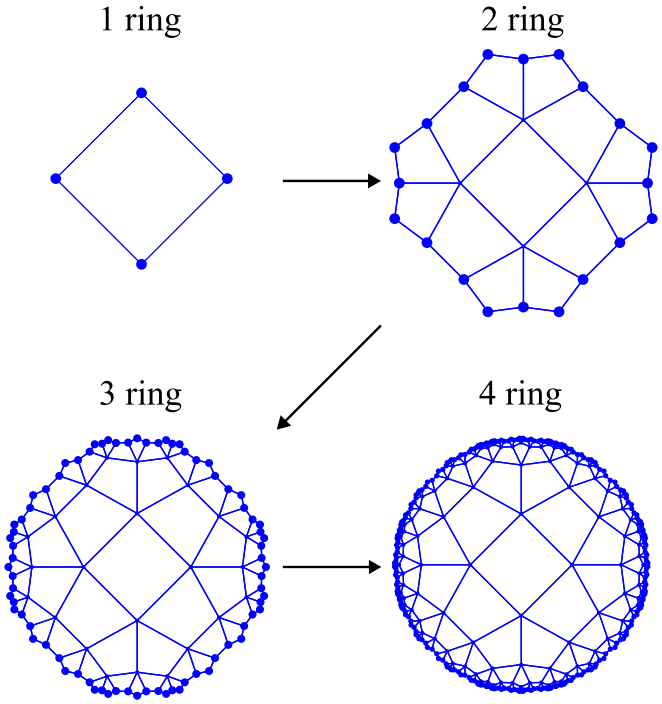

FIG. 2. Generating procedure of a $\{4, 5\}$ lattice with 1, 2, 3, and 4 rings using the vertex-inflation method. The bold sites of each lattice highlight the iteratively attached outermost ring, i.e., the boundary of that lattice.

exponentially with the number of ring, n, as $N \sim \lambda^n$, where λ is a parameter depending on specific $\{p, q\}$. In contrast, for Euclidean lattices, $N \sim n^2$. Additionally, the number of sites, N_{boun}, on the outermost ring of the hyperbolic lattice, which corresponds to the boundary, also increases exponentially with n for large n, whereas in Euclidean lattices, it increases linearly as $N_{\mathrm{boun}} \sim n$. A brief proof of these properties can be found in Appendix A, highlighting the fundamental differences between the two geometries. These properties all bring difficulties for numerical computations.

C. Partition of subsystems on the hyperbolic lattice

Since the choice of subsystem affects the EE, we now turn to specify our partition methods. When partitioning subsystems to study the EE, we need to choose the largest possible subsystems while keeping them as far from the boundary as possible to minimize the finite-size effect. However, as explained in Sec. II B, N and N_{boun} grow exponentially with n, making it difficult to have a relatively large bulk. We define R_i as the shortest discrete graph path from a bulk site i to the boundary. Sites with R larger than a certain threshold R_{min} can be chosen to form a single-connected region as A, thereby positioning the subsystem on the inner rings of the lattice. Regarding the symmetry of the subsystems, on Euclidean lattices, subsystems are typically chosen as a series of polygons similar to the overall system. However, the symmetry of a hyperbolic lattice, described by the *triangle* group and the *Fuchsian* group, is non-Abelian [55–57]. Consequently, the subsystems cannot maintain the same symmetries as on the Euclidean lattice.

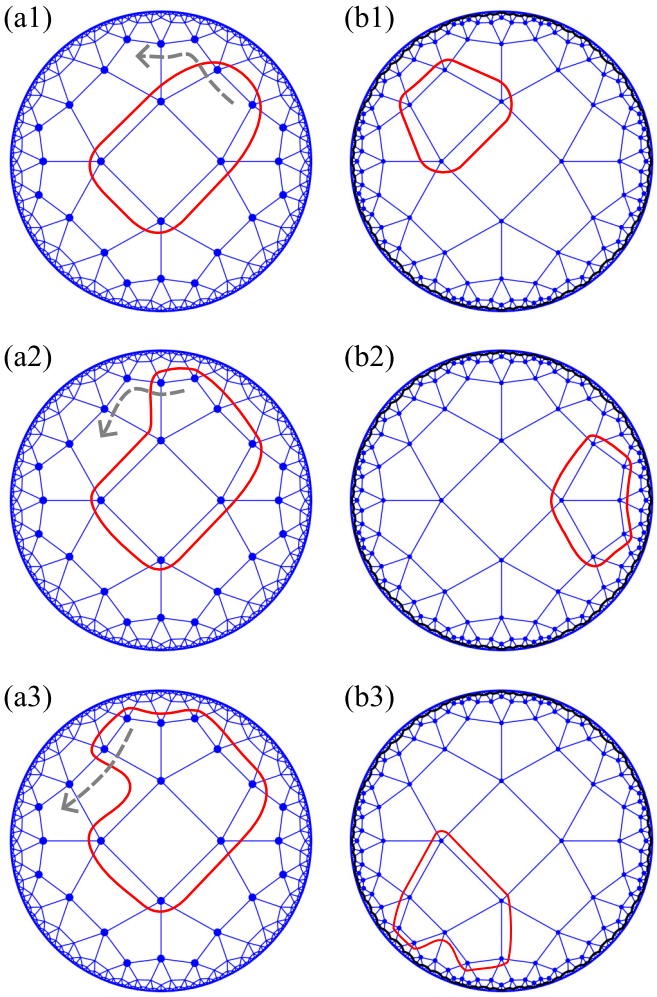

FIG. 3. Partition of subsystems on a {4, 5, 6} lattice. (a) Subsystems generated through partition I that is adopted in the main text. (b) Subsystems generated through partition II. Here we generate random subsystems of specific size: (b1) 4, (b2) 6, and (b3) 8, within the region denoted by the black line. The number of bonds connecting sites inside the subsystem to sites outside, which are cut by the red line, are defined as the boundary L_A of the subsystem.

Therefore, we employ two different partition methods in this work. We first generate a lattice of fixed size, within which we choose the sites of the innermost ring as the initial subsystem A, and then successively increase its size by adding sites of the adjacent ring to it in a clockwise or anticlockwise direction. This iterative procedure, which generates a sequential series of subsystems, is visualized in Fig. 3(a), and is referred to as partition I. Additionally, we also conduct a random partition of the subsystem. We determine a minimum $R_{\min}$ for a considered lattice $\{p, q, n\}$ and generate a subsystem within this region. We first randomly choose a p-edge polygon, then enlarge it by successively adhering p-edge polygons around sites on the boundary of the subsystem to it, and repeat this procedure until it reaches a specific size. This partition method is referred to as partition II and can be visualized in Fig. 3(b). Since the partitions do not consistently preserve the symmetries of the subsystems, we find that through partition II, the symmetries do not significantly affect the numerical results of the EE in practical computations. In the remaining part of the main text, we consistently exhibit the results of the EE computed through partition I on some lattices and provide the supplemental data in Appendix B for more details of both partition I and partition II.

D. Entanglement entropy and Widom conjecture

Next, we concisely review some basic algebras for computing the entanglement of free-fermion systems. A useful relevant material can be found in the supplemental note of Ref. [66]. For a many-body system with ground state $|\mathrm{GS}\rangle$, its density matrix is $\rho = |\mathrm{GS}\rangle\langle\mathrm{GS}|$. We partition the system into two parts as subsystem A of the overall system and its complementary B in real space, and obtain reduced density matrix ρ_A of subsystem A by tracing over B,

$$\rho_A = \mathrm{Tr}_B|\mathrm{GS}\rangle\langle\mathrm{GS}| = \frac{1}{\mathcal{Z}}\exp(-H^E), \tag{3}$$

where $\mathcal{Z}$ is a normalization constant and H^E is the entanglement Hamiltonian, from which we can obtain the EE [69–71]. If we consider free-fermion systems, H^E has the quadratic form [72–74] $H^E = \sum_{i,j\in A} c_i^\dagger h_{ij}^E c_j$, where $c_i^\dagger$ and c_i represent the fermionic creation and annihilation operators at site i, respectively. Additionally, we can rewrite the EE as a trace of the matrix function. Consider the correlation matrix $C_{ij}^A = \langle\mathrm{GS}|c_i^\dagger c_j|\mathrm{GS}\rangle$ of subsystem A which can be obtained by projection operators $C^A = \hat{R}\hat{P}\hat{R}$, where $\hat{R} = \sum_{i\in A}|i\rangle\langle i|$ and $\hat{P} = \sum_{k\in occ.}|k\rangle\langle k|$. The EE can be calculated by [71,73–78]

$$S_A = \mathrm{Tr}_A f(C^A) = \mathrm{Tr}_A f(\hat{R}\hat{P}\hat{R}), \tag{4}$$

where $f(t) = -t\ln t - (1-t)\ln(1-t)$. Hence we obtain the EE of subsystem A.

Meanwhile, for gapless systems with codimension-1 Fermi surface, the Widom conjecture provides an analytical result of the EE [12,13],

$$S_A = \frac{L_A^{d-1}\ln L_A}{(2\pi)^{d-1}}\frac{1}{12}\iint_{\partial\Gamma\times\partial\Omega}|\boldsymbol{n_r}\cdot\boldsymbol{n_p}|dS_r dS_p, \tag{5}$$

where $\partial\Gamma$ and $\partial\Omega$ denote the boundaries of the Fermi sea and the subsystem we consider, and $\boldsymbol{n_p}$ and $\boldsymbol{n_r}$ denote the exterior unit normals of these boundaries. Since the presence of a codimension-1 Fermi surface implies a finite DOS of the system, Eq. (5) also relates the DOS to the scaling coefficient. If the codimension of the Fermi surface is higher than one, the leading term of the EE exhibits area-law scaling behavior, as seen in the Dirac point of the tight-binding model on the honeycomb lattice [7,79,80]. However, the validity of Eq. (5) requires a Euclidean metric with Abelian translation symmetry and thus is not naturally applicable in the hyperbolic geometry, so we aim to provide numerical evidence in this paper.

III. ENTANGLEMENT ENTROPY SCALING OF GAPLESS FREE-FERMION SYSTEMS WITH FINITE DOS

A. Numerical study of DOS

In this section, we numerically study the scaling behavior of the EE of gapless free-fermion systems with finite DOS

on hyperbolic lattices. To begin with, we consider the gapless systems with a one-orbital tight-binding model,

$$H_1 = -t \sum_{\langle ij \rangle} (c_i^\dagger c_j + \text{H.c.}) - \mu \sum_i c_i^\dagger c_i, \tag{6}$$

where $\langle ij \rangle$ denotes the nearest-neighboring sites, t is the hopping amplitude, and μ is the chemical potential. First, we should verify that the Hamiltonian H_1 is indeed gapless. We notice that the DOS obtained through exact diagonalization for 10^4 sites still exhibits a finite-size effect, and thus it is insufficient to verify whether or not the system is gapless through it. Consequently, we analyze the DOS in the thermodynamical limit through the Haydock recursion method [62–65].

One can calculate the local DOS $\rho_i(E)$ at a site i through the Green's function,

$$\rho_i(E) = -\lim_{\epsilon \to 0^+} \frac{1}{\pi} \text{Im} \langle i | G(E + i\epsilon) | i \rangle, \tag{7}$$

where $|i\rangle$ is the state that we consider and the Green's function is $G(E) = 1/(E - H)$. The diagonal element of G can be expanded in continued fraction,

$$G_{ii}(E) = \cfrac{1}{E - a_1 - \cfrac{b_1^2}{E - a_2 - \cfrac{b_2^2}{\ddots}}}, \tag{8}$$

where the rational coefficients a_n and b_n can be numerically computed by the underlying Hamiltonian matrix H through a specific recursive relation. After introducing a proper fraction termination, we obtain $\rho_i(E)$, which is also the DOS for regular tilings up to a normalization factor [62]. By using this method, we confirm that the Hamiltonian H_1 is indeed gapless on lattices that we study here, as shown in Figs. 4(b1)–4(b4). One can refer to Appendix C for more details of this method and numerical results.

B. Numerical evidence of area-law scaling behavior of EE

To proceed further, we use our approaches detailed in Sec. II to compute the EE on various lattices, including both Euclidean and hyperbolic. In Figs. 4(c2)–4(c4), we show the results computed on $\{3, 7\}$, $\{4, 5\}$, and $\{6, 4\}$ lattices. Additionally, in Fig. 4(c1), we also include the EE computed on a Euclidean $\{4, 4\}$ lattice for comparison. More numerical results through different partition methods on different lattices are detailed in Appendix B. The finite-size scaling analysis can be found in Appendix D. The numerical analysis of the super-area law is presented in Appendix E.

First, in the Euclidean case, the EE of gapless systems with finite DOS exhibits super-area law, corresponding to our results computed on a $\{4, 4\}$ lattice in Fig. 4(c1), where we anticipate the scaling function $S_A / \ln L_A = cL_A^\alpha + d$. When we turn to the hyperbolic case, our most surprising finding is that the EE of gapless systems with finite DOS is proportional to the length of the boundary of subsystem A. We anticipate that the scaling of the EE should have $S_A = aL_A^\alpha + b$. By using the coefficient of determination, R^2, we find that $\alpha \approx 1$ is the optimal fit closest to 1, as shown in Figs. 4(c2)–4(c4). The blue lines in Fig. 4(c) show the fitting functions with $\alpha = 1$. This result indicates that the EE of gapless systems with finite DOS on hyperbolic lattices satisfies the area law by definition,

$$S_A = aL_A + \cdots, \tag{9}$$

where L_A represents the total number of bonds connecting a site inside the subsystem to a site outside the subsystem which are cut by the boundary of the subsystem A, which is consistent with the Euclidean case and visualized in Fig. 3. As the number of sites on the boundary can grow linearly with the number of sites in the subsystem in the thermodynamical limit, we discuss the volume law of EE in Appendix A.

With more numerical computations, as illustrated in Appendix B, and through the numerical analysis that excludes of the possibility of super-area-law scaling presented in Appendix E, we further confirm the existence of area law of the EE for gapless ground states with finite DOS on a hyperbolic lattice. Reference [34] recently experimentally simulated a weakly coupled scalar field to study the AdS/CFT correspondence on hyperbolic lattices. In this work, the EE behavior for entanglement-wedge subsystems of the bulk scalar field satisfies the Ryu-Takayanagi (RT) formula [19] for the connection between the EE of boundary CFT and geometry of the hyperbolic lattice, a result that also has physical understanding [17–19]. Furthermore, we want to ask why this exotic area law given by Eq. (9) of gapless free-fermion systems with finite DOS appears in the hyperbolic case. The analytical formula of the EE is based on the Widom conjecture of the asymptotic behaviors of Toeplitz matrices on the Euclidean lattice. Due to the absence of Euclidean translation invariance on hyperbolic lattice, the future analytical understanding of EE could be associated with studying the conjecture of correlation matrices with the symmetry of a hyperbolic lattice.

Moreover, following Swingle's *mode-counting* argument [14], for free-fermion systems with codimension-1 Fermi surface, the EE can be obtained by counting the contributions of 1D fermionic gapless modes near the Fermi surface perpendicular to the boundary of the subsystem in real space, where each fermionic gapless mode contributes $\ln L_A$ to the EE by adopting the calculation of CFT. Then, we obtain that EE satisfies $S_A \sim L_A^{d-1} \ln L_A$ in the Euclidean case. On a hyperbolic lattice, the Swingle's mode-counting picture is invalid due to the absence of a "Fermi surface" of the usual definition. If we can stack and count the contribution of the infinite fermionic gapless modes near the generalized Fermi surface for the EE, we can obtain the scaling behavior of the EE for hyperbolic systems. However, there is a lack of a realizable stacking and counting way on a hyperbolic lattice. According to Eq. (4), the EE depends on the projectors $\hat{P}$ and $\hat{R}$. HBT provides an insight for us into the parametrization of the generalized hyperbolic momentum space and non-Abelian Bloch states [55–57]. Therefore, our numerical simulation raises questions and challenges for HBT to obtain a generalized Widom conjecture and Swingle's mode-counting picture for hyperbolic lattices, as well as the expressions of $\hat{P}$ and $\hat{R}$ from the parameterized momentum space.

The scaling behavior of the EE is related to the nonlocal properties of the systems. Due to the absence of the logarithmic correction of the EE in Eq. (9), we realize that the gapless fermions on hyperbolic lattices should have exotic behavior owing to its nontrivial underlying hyperbolic geometry, and the study of this area law may provide perspective on

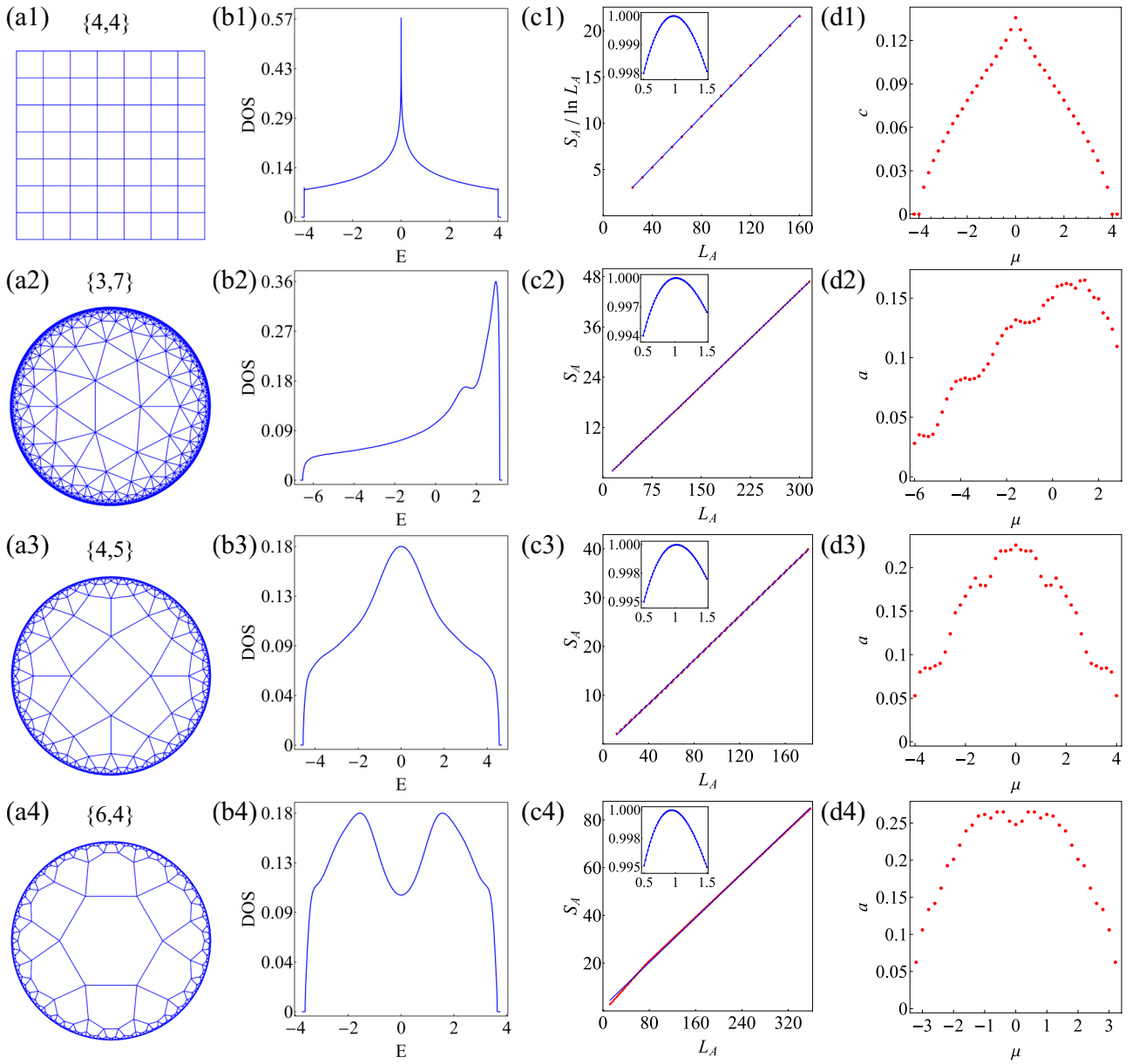

FIG. 4. Linear fit of the EE and dependence of scaling coefficients on DOS for Euclidean {4, 4} and hyperbolic {3, 7}, {4, 5}, {6, 4} lattices (rows 1 to 4, respectively) of gapless systems with Hamiltonian H_1. Column (a) shows the lattices. Column (b) shows the DOS computed by the Haydock recursion method, which gives the DOS in the thermodynamical limit of Hamiltonian H_1, with details in Appendix C. Column (c) shows the linear fit of the EE and boundary (partition I is taken and results of partition II are exhibited in Appendix B). The insets show the coefficient of determination, R^2, as a function of α. In columns (b) and (c), we set $t = 1$ and $\mu = 0$. Column (d) shows the dependence of coefficients a and c on the DOS. Columns (c) and (d) are numerically computed on {4, 4, 40} (6400 sites), {3, 7, 9} (17 328 sites), {4, 5, 6} (5400 sites), and {6, 4, 5} (10 086 sites) lattices, respectively.

the entanglement for HBT as discussed above. Additionally, as hyperbolic geometry suppresses entanglement, it is worth investigating the asymptotic behavior of the EE with respect to q and we discuss this in Appendix F. In the forthcoming Sec. III C, we will continue to discuss our numerical findings, especially focusing on the scaling coefficient.

C. Numerical study of scaling coefficient and possibility of a generalized Widom conjecture

In the Euclidean case, we know from Eq. (5) that the scaling coefficient of the super-area law is analytically determined by the flux factor $|\boldsymbol{n_r} \cdot \boldsymbol{n_p}|$ reflecting geometry of the codimension-1 Fermi surface and thus the scaling coefficient changes according to the DOS, as visualized in Fig. 4(d1). Because a hyperbolic lattice allows for generalized momentum space, we question whether the DOS can influence the coefficient a in the area law given by Eq. (9) following the Euclidean scenario.

We compute the EE for Hamiltonian H_1 with $t = 1$ and different chemical potential μ on different hyperbolic lattices. Figures 4(d2)–4(d4) show the dependence of the scaling coefficient a on μ. Compared to the DOS computed in Figs. 4(b2)–4(b4), we can directly see that the scaling

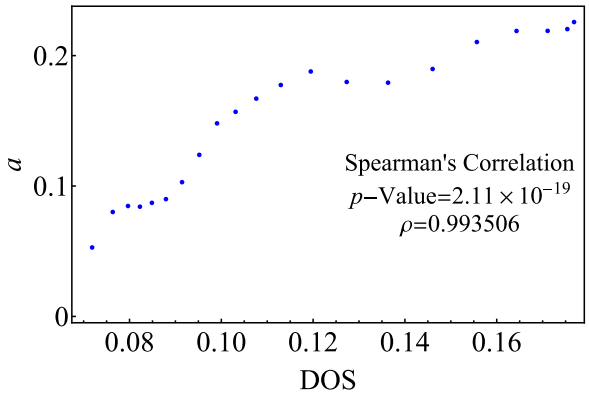

FIG. 5. Dependence of coefficient a on the DOS of a $\{4, 5, 6\}$ lattice, computed for Hamiltonian H_1 with $t = 1$ and $\mu \in [0, 4]$. The p-value approaching 0 and ρ approaching 1 of the Spearman's correlation verifies the approximately positive correlation between the scaling coefficient and DOS, suggesting that a generalized Widom conjecture may exist.

coefficient a is correlated to the DOS. In Fig. 5, we present the result of a computed on the $\{4, 5, 6\}$ lattice as an example, where the Spearman's correlation indicates the approximately positive correlation between a and the DOS. Notably, from Fig. 4, we can see that a and the DOS do not completely coincide. This discrepancy might also be due to the finite-size effect, as the EE computed here is obtained from a finite lattice, while the DOS is obtained in the thermodynamical limit.

Remarkably, the scaling coefficient a is nonuniversal and influenced by many factors such as partition and lattice configuration, but the approximately positive correlation between a and the DOS implies that a generalized momentum space and Fermi surface might play a role in determining a, similar to its Euclidean counterpart. In the Euclidean system, the validity of the Widom conjecture and Swingle's mode-counting picture need a Euclidean metric and the momentum space with dimension equal to the real-space dimension due to the flux factor $|\boldsymbol{n_r} \cdot \boldsymbol{n_p}|$ in Eq. (5) counting the number of fermionic modes perpendicular to the real-space boundary of the subsystem. In fact, the translation group of the hyperbolic lattice is typically non-Abelian, resulting in the existence of higher-dimensional ($d \geqslant 2$) irreducible representations of translation group and non-Abelian Bloch states. Meanwhile, even for the 1D irreducible representations, the dimension of the generalized momentum space can be $d > 2$ [55–57], which is larger than the spatial dimension of the lattice, and thus Swingle's argument breaks down directly. To exactly obtain a description of reciprocal space of a hyperbolic lattice, one needs to know about the higher-dimensional representations. It is an open question as to whether we can obtain a generalized Widom conjecture and Swingle's mode-counting picture for a hyperbolic lattice.

IV. ENTANGLEMENT ENTROPY SCALING OF GAPPED FREE-FERMION SYSTEMS

In this section, we study EE in gapped systems. We consider the gapped systems by studying a two-orbital tight-binding model,

$$H_2 = -\sum_i t_1 (c^\dagger_{s,i} c_{p,i} + \text{H.c.}) - \sum_{\langle ij \rangle} t_2 (c^\dagger_{s,i} c_{s,j} - c^\dagger_{p,i} c_{p,j}), \tag{10}$$

where $c^\dagger_{s(p),i(j)}$ represents the fermionic creation operator at the $s(p)$ orbital of site $i(j)$. t_1 and t_2 are hopping amplitudes. We can still use the Haydock recursion method to compute the DOS and verify that H_2 is gapped, as we did in Sec. III. For instance, in Fig. 7(a), we show the DOS of Hamiltonian H_2 with $t_1 = 1$ and $t_2 = 1$ on a $\{4, 5\}$ lattice, which lead to a gapped region $[-1, 1]$.

Next, we turn to study EE in the gapped case. On a Euclidean lattice, the EE of gapped systems scales as area law $S_A = aL_A^\alpha + \cdots$. As an analogy, we also use the fitting function $S_A = aL_A^\alpha + b$ for the case on hyperbolic lattices. In Fig. 6, we show results of the EE computed on both Euclidean and hyperbolic lattices. The chosen hyperbolic lattices $\{3, 7\}$, $\{4, 5\}$, and $\{6, 4\}$ have one more adjacent site per lattice site compared to their Euclidean counterparts $\{3, 6\}$, $\{4, 4\}$, and $\{6, 3\}$, respectively. The numerical results consistently show that when the the system is gapped, the optimal fit is obtained with $\alpha \approx 1$ where R^2 is closest to 1. The blue lines in Fig. 6 show the fitting functions with $\alpha = 1$. This means that the EE scales linearly with the subsystem's boundary L_A,

$$S_A = aL_A + \cdots . \tag{11}$$

Therefore, the EE still scales according to the area law in gapped systems on a hyperbolic lattice.

Additionally, on Euclidean lattices, the coefficient a decreases as the energy gap increases. This leads us to question whether the energy gap is related to the behavior of the EE. In Fig. 7(b), we study the relation between the EE and energy gap on a $\{4, 5, 6\}$ lattice. We modulate t_1 and thus change the energy gap of H_2 from 1 to 12 and compute the EE. We find that a is negatively correlated with the system's energy gap. Analytical work on the one-dimensional gapped system has provided a rigorous relationship between the coefficient a and the energy gap [2,81]. However, the exact relationship between the scaling coefficient a and the energy gap is still a difficult question in dimension $d \geqslant 2$. In our results, we do not find a functional relationship that can physically explain the relationship between the coefficient a and the energy gap in the hyperbolic case, but the observed negative monotonic relationship between them suggests a similarity to the Euclidean case.

Overall, our numerical data computed in gapped systems demonstrate that the EE scales according to the area law as in Eq. (11). This aligns with our expectations from the Euclidean case, suggesting that the gapped scenario in the hyperbolic case is not particularly unique.

V. DISCUSSIONS

In this paper, we have numerically studied the scaling behavior of entanglement entropy of gapped free fermions as well as gapless free fermions with finite DOS on hyperbolic lattices. We find that for both gapped and gapless systems, the EE scales according to a rigorous area-law scaling

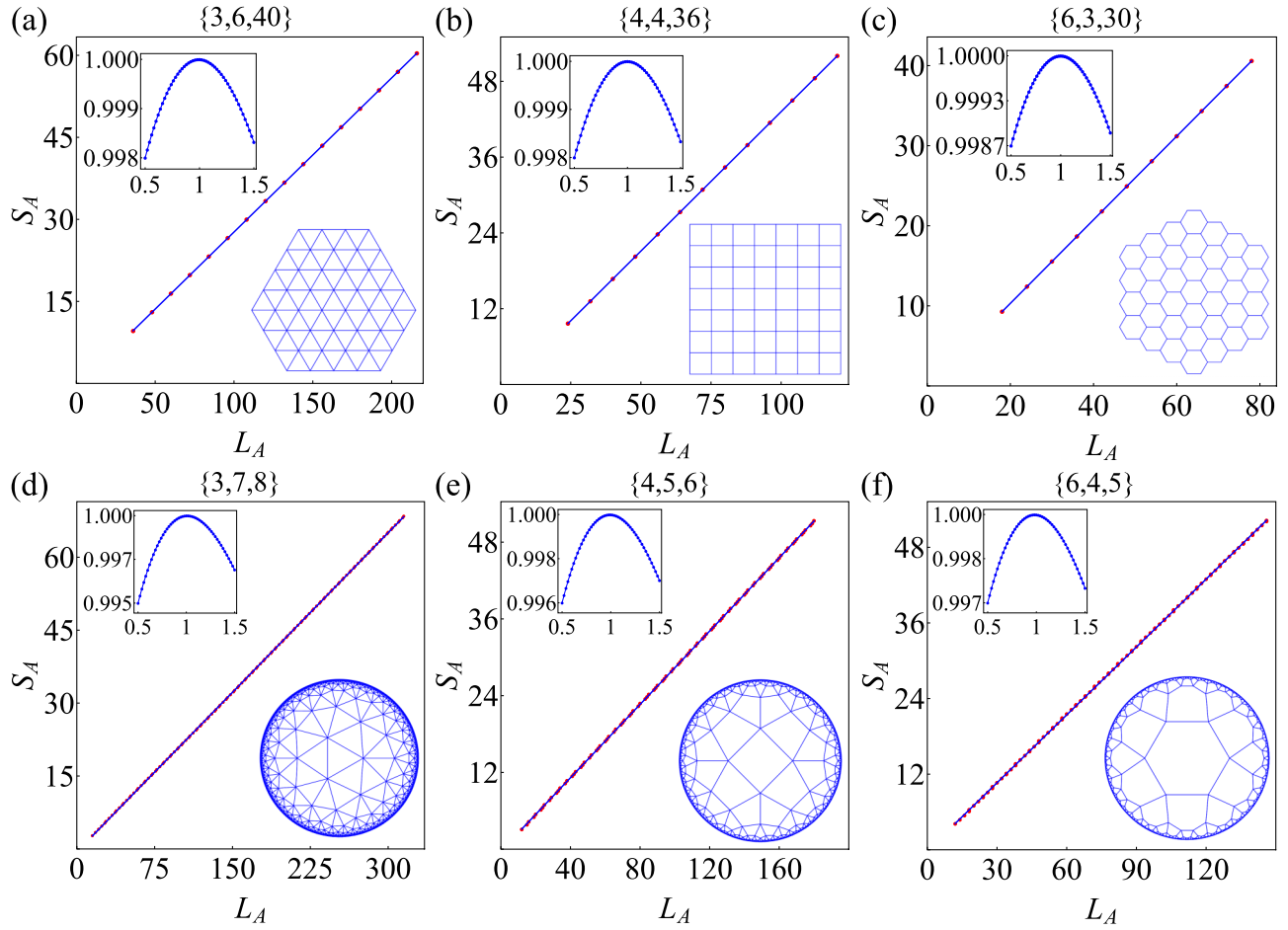

FIG. 6. Linear fit of the EE in the gapped case with Hamiltonian H_2 on (a) {3, 6, 40} (4800 sites), (b) {4, 4, 36} (5184 sites), (c) {6, 3, 30} (5400 sites), (d) {3, 7, 8} (6615 sites), (e) {4, 5, 6} (5400 sites), and (f) {6, 4, 5} (10 086 sites) lattices which have two orbitals at a site. The fittings show the area law of the EE. The insets show R^2 as a function of α. Such a linear dependence of S_A on L_A is consistent with the Euclidean case. The hopping amplitude of H_2 is set to $t_1 = 1$ and $t_2 = 1$.

$S_A = aL_A + \cdots$. Although the gapped case fulfills our expectation in Euclidean geometry, the super-area law in gapless systems breaks down in contrast. Additionally, the scaling coefficient of the area law in gapless systems is positively correlated to the DOS. This scaling behavior of the EE is unique

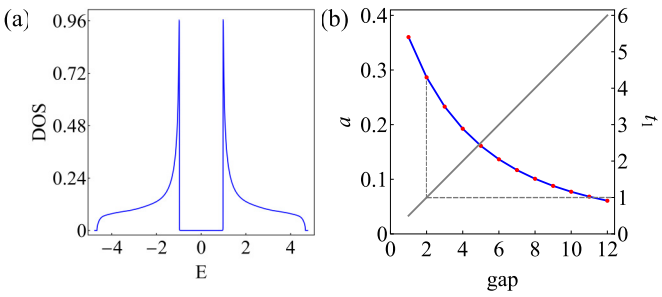

FIG. 7. DOS and EE computed on a {4, 5} lattice for Hamiltonian H_2. (a) DOS computed by the Haydock recursion method. The hopping amplitude $t_1 = 1$ and $t_2 = 1$ leads to a gapped region $[-1, 1]$. (b) Scaling coefficient a of the area law varies with different energy gaps, computed on a {4, 5, 6} lattice. The gray line shows the energy gap modulated by t_1.

in hyperbolic geometry. On a Euclidean lattice, the super-area law of gapless free fermions with finite DOS demonstrates that the entanglement is enhanced by the fermionic statistics and the quantum correlation of the infinite fermion modes near the Fermi surface [12,14]. These observations show that the underlying geometry can significantly influence the entanglement behavior of ground states of free-fermion systems, similar to our previous findings in fractal geometry [15], as summarized in Table I. Compared to the Euclidean case, the area law reveals the presence of exotic properties of fermions on a hyperbolic lattice. The further study of this area law might raise the question for a generalized conjecture of correlation matrices with symmetry of a hyperbolic lattice, while the possibility of generalization of Swingle's argument for the EE to the hyperbolic case through HBT also merits future research [55–57].

Notably, many studies suggest the relationship between the entanglement and the geometry of AdS space, particularly in the context of hyperbolic lattices [34,36–38]. Reference [34] experimentally studies AdS/CFT correspondence, confirming that the EE for the entanglement wedge as a subsystem of a bulk weakly coupled scalar field is consistent with the RT formula [19]. Inspired by the experimental progress, the

experimental simulation of Gaussian fermionic field theory to study EE is worthy of further study. Additionally, numerical studies of spin models also point out the nontrivial behaviors of correlation functions and entanglement of spin models on hyperbolic lattices [36–38]. Based on our numerical results and these works, along with the theoretical research on the relationship between EE and AdS space geometry, the investigation within the framework of field theory and holography to understand the area-law EE of ground states for free-fermion systems on a hyperbolic lattice is an interesting topic for future work [17–23].

As it is feasible to simulate entanglement experimentally [66] while the experimental simulation of hyperbolic lattices has been achieved [30–35], this may provide us with a novel approach to study the geometry of the quantum system through entanglement. Furthermore, the area law of EE in both gapped and gapless systems suggests that it is efficient to study correlated systems on hyperbolic lattices with gapless emergent fermions by tensor-network-type numerical techniques [25,67,68]. We hope that our work can provide some inspiration to related fields in the future. Another interesting future direction is to study the entanglement of non-Hermitian systems [77,78,82–100] on hyperbolic lattices, which is much more practical in, e.g., phononic systems where gain and loss are natural.

ACKNOWLEDGMENTS

This work was in part supported by National Natural Science Foundation of China (NSFC) Grants No. 12474149 and No. 12074438. The calculations reported were performed on resources provided by the Guangdong Provincial Key Laboratory of Magnetoelectric Physics and Devices, Grant No. 2022B1212010008.

APPENDIX A: HYPERBOLIC LATTICE

In this Appendix, we give details of constructing hyperbolic lattices discussed in Sec. II. Additionally, we discuss the geometrical properties of a hyperbolic lattice as well as the volume law of EE.

1. Vertex-inflation method of generating hyperbolic lattice

The vertex-inflation method or vertex-inflation tiling procedure for generating a hyperbolic lattice was first purposed in the field of hyperbolic tensor-network theory [60,61] and then optimized for study in lattice many-body models [48]. Here, we introduce our lattice setup based on this method.

To start with, we generate a regular p-edge polygon at the center of the Poincaré disk and denote it as the first *ring* of the lattice. We then attach new sites to the first ring to form a new ring, and iteratively repeat this procedure. These finite-size lattices, named as flakes, can be divided into rings in order and every regular p-edge polygon is denoted as a *tile*. For every vertex of a tile, the vertex is affiliated to this tile. If a vertex does not have q affiliated tile, it is an *open vertex*. A vertex with q neighboring vertices does not equal to "not open" since it may have less-than-q affiliated tiles. If an open vertex has a nearest-neighboring vertex which is also open, the edge linking them is an *open edge*. The lattice setup procedure is summarized as follows:

(1) For a $\{p, q, n\}$ lattice, we find all open vertices and their corresponding open edge on its outermost nth ring. A vertex on the nth ring can either have zero or two open edges of which it is an endpoint.

(2) For every open vertex i and one of its open edges, if its number of affiliated tiles is less than $q-1$, we identify the tile to which the open edge belongs and invert this tile. This process creates a new tile and an new open edge of which i is an endpoint.

(3) Otherwise, for every open vertex with $q-1$ affiliated tiles, we identify both open edges that it belongs to and generate a new tile based on them.

(4) Go back to step (1) and repeat the whole process until all vertices on the nth ring are no longer open. So far, we have constructed a new ring and $\{p, q, n+1\}$ lattice.

By using the above method, we can construct the entire lattice, ring by ring. The procedure can be visualized by Fig. 2. The finite lattice generated by this method does not have dangling sites on the inner rings and it is natural to define the outermost ring as the boundary.

2. Exponential growth of the size of the hyperbolic lattice

In this section, we give a brief proof of the exponential growth of the size of the hyperbolic lattice. We start by considering a $\{p, q\}$ lattice with $p \geqslant 4$ and $q \geqslant 5$. The proofs for the remaining cases are similar to the following proof.

For a $\{p, q, n-1\}$ lattice, all vertices on the outermost $(n-1)$-th ring can have either two or three nearest-neighboring vertices to which is connected by an edge. We denote N_n as the number of vertices on the nth ring. The number of vertices having two nearest-neighboring vertices on the outermost ring is denoted as $N_{n-1,2}$, and the number of vertices having three nearest-neighboring vertices on the outermost ring is denoted as $N_{n-1,3}$ by analogy. Thus, we have

$$N_{n-1} = N_{n-1,2} + N_{n-1,3} \tag{A1}$$

for any $n \geqslant 2$.

In the procedure of generating the lattice, the construction of the nth ring is only dependent on the $(n-1)$-th ring. Every 2-neighboring vertex on the $(n-1)$-th ring directly has $q-2$ neighboring vertices on the nth ring, and these $q-2$ vertices form $q-3$ tiles which need $p-3$ new vertices each. Similarly, every 3-neighboring vertex on the $(n-1)$-th ring directly has $q-3$ neighboring vertices on the nth ring. These new neighboring vertices form $q-3$ tiles which need $p-3$ new vertices each.

In addition, the edges on the $(n-1)$-th ring, whose number is equal to N_{n-1}, form N_{n-1} tiles, each of which requires $p-4$ new vertices. Summarizing the above constraints, we have

$$\begin{aligned} N_n =& (p-4)N_{n-1} + (q-2)N_{n-1,2} + (p-3)(q-3)N_{n-1,2} \\ &+ (q-3)N_{n-1,3} + (p-3)(q-4)N_{n-1,3}. \end{aligned} \tag{A2}$$

We also notice that each 3-neighboring vertex on the $(n-1)$-th ring is directly connected to a vertex on the $(n-2)$-th ring. That is,

$$N_{n-1,3} = (q-3)N_{n-2,3} + (q-2)N_{n-2,2},$$

TABLE II. Lattice construction by rings. This table shows the total number of sites on the nth ring of different lattices.

Lattice	First	Second	Third	Fourth	Fifth	Sixth
{3, 7}	3	12	33	87	228	597
{4, 5}	4	20	76	284	1060	3956
{6, 4}	6	42	246	1434	8358	48714
{8, 3}	8	40	152	568	2120	7912
{8, 8}	8	280	9512	323128		
Lattice	First	Fifth	10th	100th		
{3, 6}	3	27	57	597		
{4, 4}	4	36	76	796		
{6, 3}	6	54	114	1194		

for any $n \geqslant 3$. And for the 2-neighboring vertex, the case is

$$N_{n-1,2} = (p-4)N_{n-2} + (p-3)(q-3)N_{n-2,2} + (p-3)(q-4)N_{n-2,3}.$$

Summarizing the above results, we get the recursive relation,

$$N_n = (pq - 2p - 2q + 2)N_{n-1} - N_{n-2}. \tag{A3}$$

Solving this relation is equivalent to finding the root of the quadratic equation

$$x^2 - (pq - 2p - 2q + 2)x + 1 = 0, \tag{A4}$$

for x. As we directly have $N_1 = p$ and $N_2 = p^2q - 2pq - 2p^2 + 3p$, by solving the above equation, we find the formula of N_n as

$$N_n = \frac{p}{2^{n+1}}\left(-1 - \sqrt{\frac{t}{t-4}}\right)(t - 2 - \sqrt{t(t-4)})^n + \frac{p}{2^{n+1}}\left(-1 + \sqrt{\frac{t}{t-4}}\right)(t - 2 + \sqrt{t(t-4)})^n, \tag{A5}$$

where $t = (p-2)(q-2) > 4$. Finally, summing over all the rings yields the exponentially growing size of the $\{p, q, n\}$ lattice,

$$N \sim \lambda^n, \tag{A6}$$

where λ depends on specific p, q and can be analytically calculated.

This shows an exponential growth of the lattice size which is absolutely different from the Euclidean case since a Euclidean lattice grows as $N \sim n^2$. Some lattices are shown in Table II, from which we can see the difference between the hyperbolic case and Euclidean case.

3. Entanglement volume law on hyperbolic lattice

In this section, we show that L_A of a subsystem approaches a finite fraction of the total number of lattice sites in the subsystem $N(V_A)$ in the thermodynamical limit $n \to \infty$, and discuss the volume law of EE on a hyperbolic lattice.

Consider a $\{p, q, n\}$ lattice as a subsystem A in a larger lattice. The L_A defined in Sec. II B can be expressed as

$$L_A = (q-2)N_{n,2} + (q-3)N_{n,3}. \tag{A7}$$

By solving for $N_{n,2}$ and $N_{n,3}$ similar to the approach in Appendix A 2, we find that the leading-order terms of $N_{n,2}$ and $N_{n,3}$ coincide with those of N_n. Therefore, L_A/N becomes a finite fraction for sufficiently large subsystems or in the thermodynamical limit $n \to \infty$, e.g., approximately 1.732 for the {4, 5} lattice.

The area law indicates that the EE is proportional to the degrees of freedom $dN(L_A^{D-1})$ on the boundary of the subsystem, where d is the local Hilbert space on a lattice site, D is the spatial dimension, and $N(L_A^{D-1})$ is the number of boundary lattice sites of the subsystem. In Euclidean geometry, $N(L_A^{D-1})$ is proportional to the boundary area L_A^{D-1}, where L_A is the linear size of the subsystem [7]. Meanwhile, $N(L_A^{D-1})$ is equal to the total number of lattice bonds connecting the lattice sites in two complementary subsystems. Therefore, the scaling $S_A \sim L_A^{D-1}$ is referred to as the area law. In our work presented here, we also adopt the total number of bonds as the linear size L_A, as clarified in Sec. III B, and numerically find that the scaling $S_A \sim L_A$ still holds for both gapless (with finite DOS) and gapped free-fermion systems on hyperbolic lattices. Hence, we refer to this scaling on hyperbolic lattices as the area law.

The volume law indicates that the EE is proportional to the total degrees of freedoms $dN(V_A)$ within the subsystem, where $N(V_A)$ is the total number of lattice sites in the subsystem. In Euclidean geometry, $N(V_A)$ is proportional to the volume $V_A \sim L_A^D$ of the subsystem. Therefore, the scaling $S_A \sim L_A^D$ is referred to as the volume law. On hyperbolic lattices, however, the area of a region can scale as a finite fraction of its volume in the asymptotic limit (i.e., for sufficiently large subsystems), leading to $V_A \sim L_A$ geometrically. Consequently, on hyperbolic lattices, the area law can also be interpreted as $S_A \sim L_A \sim V_A$, which may alternatively be referred to as the volume law. However, to ensure that the definition of area law is consistent on both Euclidean and hyperbolic lattices, we still regard the scaling $S_A \sim L_A$ on hyperbolic lattices as the area law.

APPENDIX B: SUPPLEMENTAL DATA OF NUMERICAL COMPUTATIONS OF EE THROUGH PARTITION I AND PARTITION II

As detailed in Sec. II, when studying EE, we use some different partition methods to investigate how the EE varies with the boundary L_A as the size of the subsystem changes.

The supplemental data of EE computed through partition I with $t = 1$ and $\mu = 0$ for Hamiltonian H_1 on lattices different from those in the main text can be seen in Fig. 8. Here we anticipate the scaling function $S_A/\ln L_A = cL_A^\alpha + d$ for the Euclidean {3, 6} lattice which exhibit super-area law that can be seen in Fig. 8(a), while the hyperbolic cases all exhibit area law and we anticipate the scaling of EE is $S_A = aL_A^\alpha + b$. On Euclidean lattices, successively increasing the subsystems' size can result in many subsystems with different shapes and sizes sharing the same L_A, e.g., the {3, 6} lattice in Fig. 8(a). In the main text, the size of the subsystem on Euclidean lattices grows discretely so that we have subsystems similar to the overall system. However, successively enlarging the size of the subsystem causes L_A to successively increase in the hyperbolic case, as shown in Figs. 8(b)–8(f). This enables

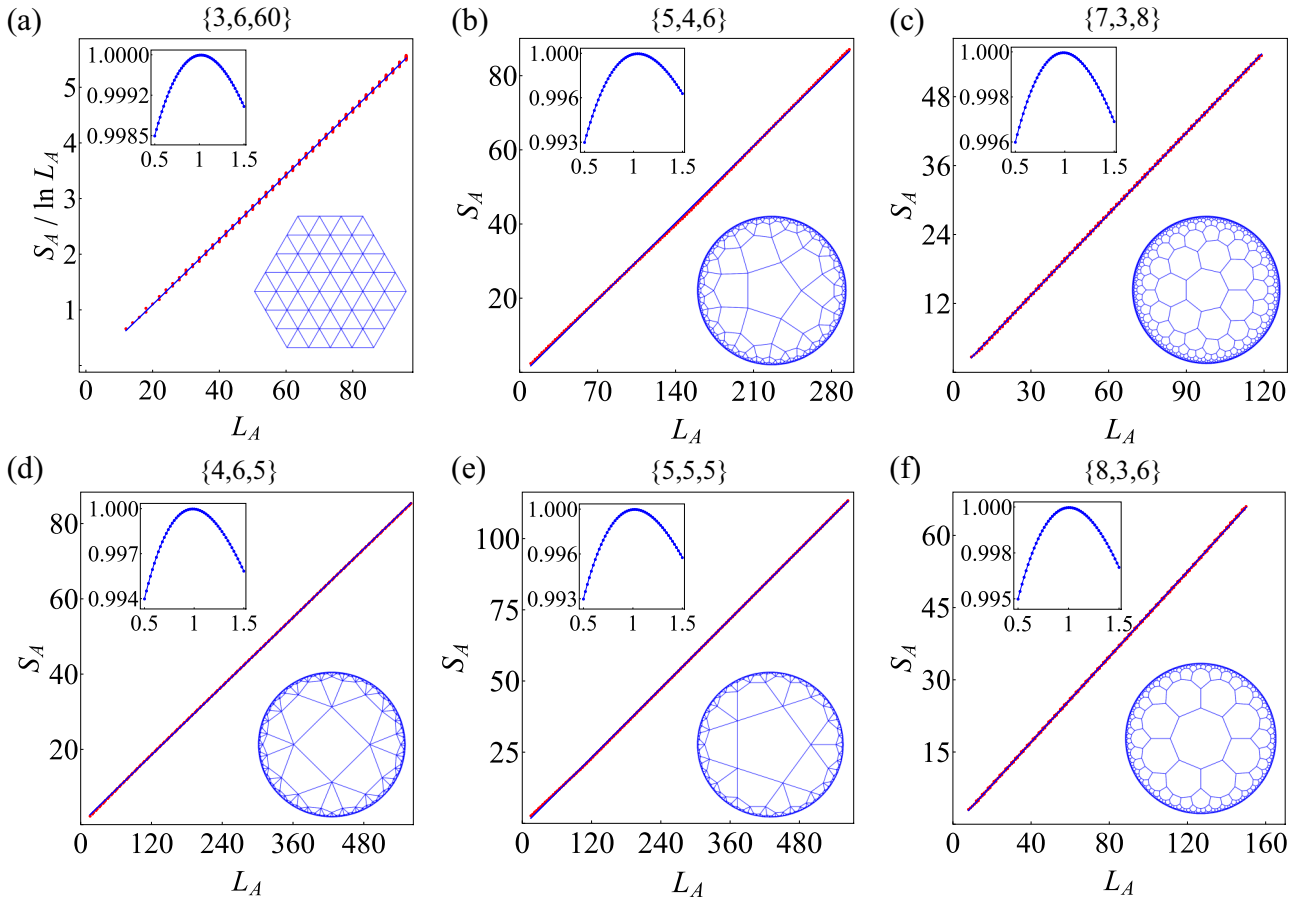

FIG. 8. Results of the EE scaling fit for Hamiltonian H_1 with $t = 1$ and $\mu = 0$. Subsystems are generated through partition I for different lattices. On the Euclidean lattice (a) {3, 6, 60} (10 800 sites), the inset shows R^2 as a function of α in the fitting function $S_A/\ln L_A = cL_A^\alpha + d$, while R^2 as a function of $S_A = aL_A^\alpha + b$ in the remaining hyperbolic cases (b) {5, 4, 6} (6750 sites), (c) {7, 3, 8} (15 435 sites), (d) {4, 6, 5} (6724 sites), (e) {5, 5, 5} (15 125 sites), and (f) {8, 3, 6} (10 800 sites). All hyperbolic cases correspond with the area law.

us to study the growth of EE with the successively increasing boundary with numerous data, regardless of the exponential wall of the lattice size. Although this partitioning method may not maintain the symmetries, it still significantly distinguishes between area-law and super-area-law behavior of the EE.

The results of the EE computed through partition II are exhibited in Fig. 9, where we use the fitting function $S_A = aL_A^\alpha + b$. Because choosing subsystems too close to the boundary will cause a finite-size effect, we define an internal region of the lattice, specify the size of the subsystems, and then randomly choose subsystems that can be composed of connected tiles. The results in Fig. 9 are computed with Hamiltonian H_1 and we set $t = 1$ and $\mu = 0$, as are those shown in Fig. 8, and the blue lines show the fitting functions with $\alpha = 1$. Even with the same size or the same L_A, subsystems partitioned through this method can have various possible shapes and do not maintain the same symmetries. However, the symmetries of these subsystems do not affect the scaling behavior of the EE. From the results, we find that linearity still demonstrates that the best description between the EE and boundary is the area law.

APPENDIX C: NUMERICAL STUDY OF DOS

Based on our considerations in the main text, we need to verify that the Hamiltonian H_1 is indeed gapless on the lattices that we considered. Because the geometric properties of a hyperbolic lattice induce exotic behavior of free fermions, we use the DOS as the verification.

Additionally, as aforementioned, the size of the system grows exponentially with n, resulting in numerical difficulties in the exact-diagonalization (ED) approach. Therefore, we use the Haydock recursion method [62–65,101,102] to acquire the DOS in the thermodynamical limit.

1. Haydock recursion approach to DOS

We can calculate the local density of states (LDOS) at a particular site j by the Green's function,

$$\rho_j(E) = -\lim_{\epsilon\to 0^+}\frac{1}{\pi}\mathrm{Im}\langle j|G(E+\mathrm{i}\epsilon)|j\rangle. \tag{C1}$$

The Green's function $G_{ij}(E) = \langle i|(E-H)^{-1}|j\rangle$ can be decomposed into contributions from moments of the Hamiltonian $G_{ij}(E) = E^{-1}\langle i|1 + \sum_n H^n/E^n|j\rangle$.

The Haydock recursion method [63–65], also known as the continued-fraction method, gives a method to compute the diagonal matrix element of $G(E)$,

$$G_{jj}(E) = \langle l_1|G(E)|l_1\rangle = \cfrac{1}{E - a_1 - \cfrac{b_1^2}{E - a_2 - \cfrac{b_2^2}{\ddots}}}. \tag{C2}$$

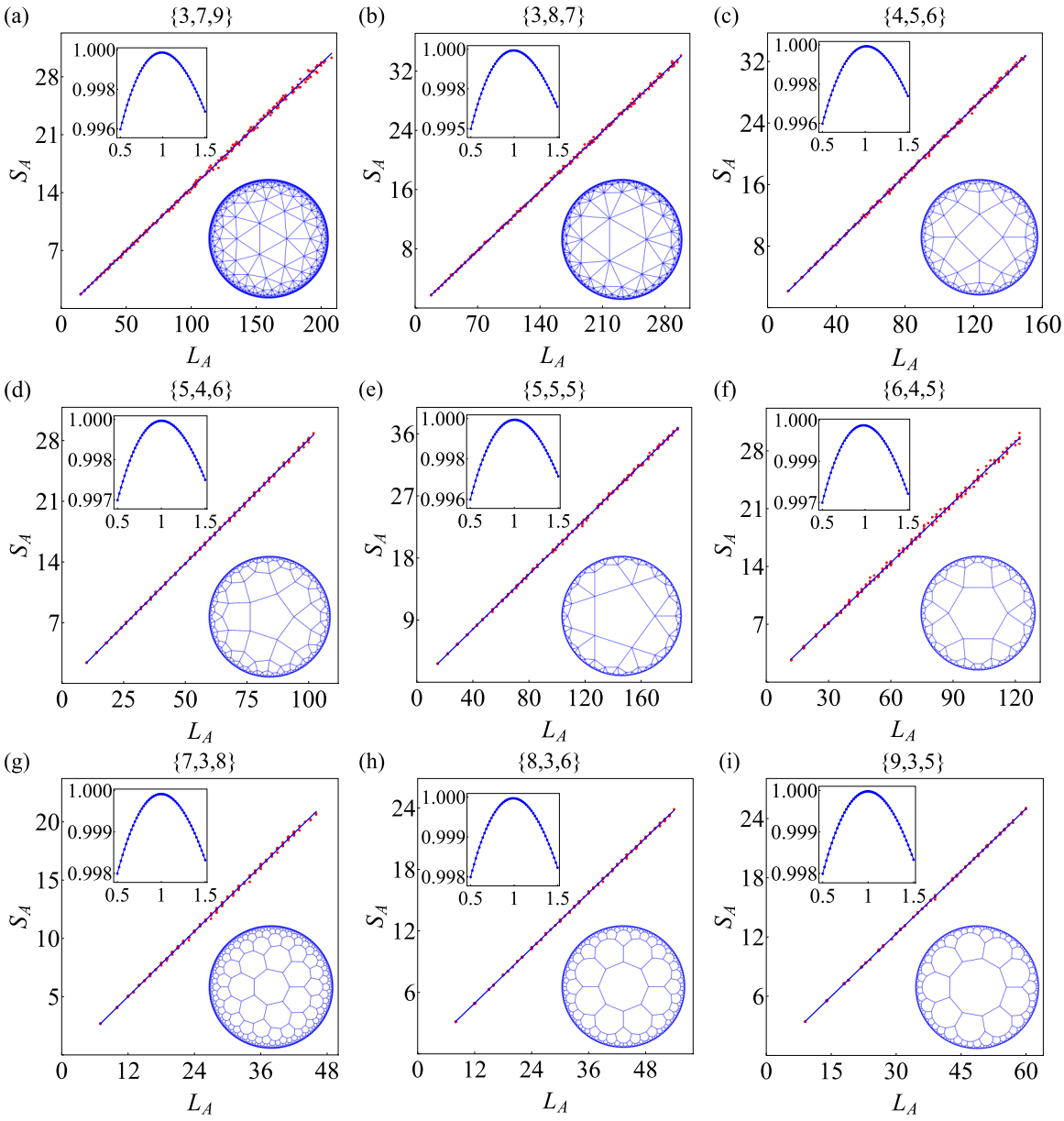

FIG. 9. Results of the EE scaling fit for Hamiltonian H_1 with $t = 1$ and $\mu = 0$, including (a) {3, 7, 9} (17 328 sites), (b) {3, 8, 7} (15 123 sites), (c) {4, 5, 6} (5400 sites), (d) {5, 4, 6} (6750 sites), (e) {5, 5, 5} (15 125 sites), (f) {6, 4, 5} (10 086 sites), (g) {7, 3, 8} (15 435 sites), (h) {8, 3, 6} (10 800 sites), and (i) {9, 3, 5} (7569 sites) lattices. Subsystems are generated through partition II for different hyperbolic lattices. The insets show R^2 as a function of α in the fitting function $S_A = aL_A^\alpha + b$.

Here, $|l_1\rangle$ is a unit vector that has a nonzero component at site j only. The rational continued-fraction coefficients a_i and b_i in Eq. (C2) can be obtained by the following recursive relation:

$$\begin{aligned} a_i &= \langle l_i|H|l_i\rangle \\ |n_{i+1}\rangle &= (H - a_i)|l_i\rangle - b_{i-1}|l_{i-1}\rangle \\ b_i &= \sqrt{\langle n_{i+1}|n_{i+1}\rangle} \\ |l_{i+1}\rangle &= \frac{1}{b_i}|n_{i+1}\rangle, \end{aligned} \tag{C3}$$

where $i = 1, 2, 3, \ldots$ and $b_0 = 0$. For gapless systems, the coefficients a_i and b_i converge to the asymptotic value a_∞ and b_∞ for sufficiently large lattices and give the band edges

$$E_\pm = a_\infty \pm 2b_\infty. \tag{C4}$$

For gapped systems with a single band gap, which is the case of Hamiltonian H_2, the coefficients b_i converge to two asymptotic limits $\bar{b}$ and $\underline{b}$ when $n \to \infty$ [101],

$$E_+ - E_- = 2(\bar{b} + 2\underline{b}), \quad \Delta = 2(\bar{b} - 2\underline{b}), \tag{C5}$$

where Δ is the band gap.

To accurately compute the rational coefficients a_n and b_n to the order n, the shortest graphic path from site j to boundary R_j as defined in Sec. II should be at least n. Then we introduce

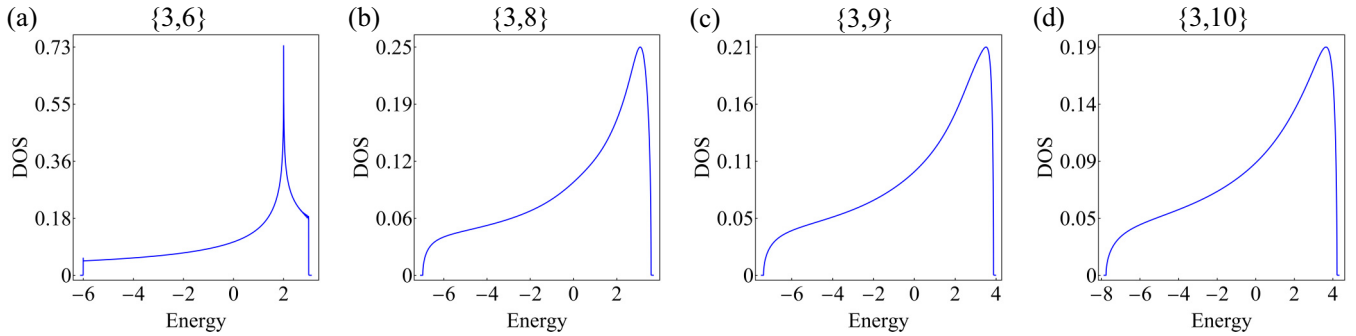

FIG. 10. Normalized DOS computed by the Haydock recursion method for Hamiltonian H_1 with $t = 1$ and $\mu = 0$. The lattices chosen here share the same $p = 3$ with $q = 6, 8, 9, 10$, while $\{3, 7\}$ has been shown in Fig. 4(b2). Through this method, we verify that these systems are indeed gapless.

a proper fraction termination,

$$t(E) = \frac{E - a_\infty - \sqrt{(E - a_\infty)^2 - 4b_\infty^2}}{2b_\infty^2}, \tag{C6}$$

for Hamiltonian H_1, where a_∞ and b_∞ are chosen as the converged a_n and b_n for large n. In a gapped system, the fraction termination can be more complicated [101,102]. For Hamiltonian H_2, we use

$$t(E) = \frac{(E - A)^2 + A^2 - B + 2b_\infty^2 - X(E)}{2b_\infty^2[(E - A) + (a_\infty - A)]}, \tag{C7}$$

where $A = \frac{1}{4}\sum t_i$, $B = \frac{1}{4}\sum t_i^2$, $X = \prod\sqrt{E - t_i^2}$, and t_i, $i = 1 \ldots 4$, are band edges which can be obtained by the asymptotic coefficient in Eq. (C5).

After deciding the termination, the LDOS at site j is given by Eq. (C1) and Eq. (C2). Since, for regular tilings, sites in the bulk are all equivalent if the lattice is sufficiently large, the LDOS is the DOS up to a normalization factor [62].

2. Numerical results of DOS

We show some results of the DOS which are computed on different lattices with up to 10^7 sites for Hamiltonian H_1 in Fig. 10. Here we compute DOS on $p = 3$ lattices and verify that they are gapless. Since this method's memory consumption scales linearly with the lattice size, it significantly exceeds the computational limits of ED methods. This method can be applied to an arbitrarily large lattice (one can obtain the result for a lattice size up to 10^9 sites [62]), but our results here are sufficient to determine whether the system is gapped or gapless in the thermodynamical limit.

We notice that the thermodynamical DOS obtained through this method is different from that computed on finite lattices through ED, indicating that the computation of the EE may exhibit a finite-size effect.

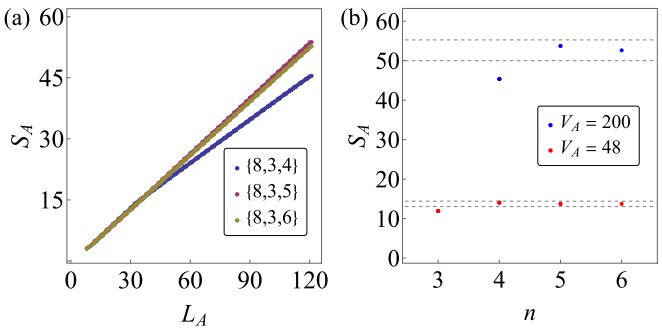

FIG. 11. Finite-size scaling analysis of the EE by the example of a $\{8, 3\}$ lattice. (a) The EE for the same subsystems computed on a $\{8, 3, n\}$ lattice with $n = 4, 5, 6$. (b) The EE for two specific subsystems ($V_A = 48$ and 200 sites) computed on a $\{8, 3, n\}$ lattice, where dashed lines show $\pm 5\%$ intervals of the EE computed on a $\{8, 3, 6\}$ lattice. Results are computed for Hamiltonian H_1 with $t = 1$ and $\mu = 0$.

APPENDIX D: FINITE-SIZE SCALING ANALYSIS OF EE

As we focus on the EE for subsystems in the bulk, in this appendix, we perform the finite-size scaling analysis to demonstrate that the boundary effect is considered in our numerical computations. We take the $\{8, 3\}$ lattice for Hamiltonian H_1 with $t = 1$ and $\mu = 0$ as an example. In Fig. 11(a), we show the EE for the same subsystems (partition I is taken) computed on a $\{8, 3, 4\}$ (768 sites), $\{8, 3, 5\}$ (2888 sites), and $\{8, 3, 6\}$ (10 800 sites) lattice, respectively, where the largest subsystem studied here is identical to the $\{8, 3, 3\}$ lattice ($V_A = 200$ sites). The optimal fit is obtained when α in the fitting function $S_A = aL_A^\alpha + b$ equals 0.859, 1.010, and 0.997 for the $\{8, 3, 4\}$, $\{8, 3, 5\}$, and $\{8, 3, 6\}$ lattice, respectively. In Fig. 11(b), two specific subsystems, identical to the $\{8, 3, 2\}$ ($V_A = 48$ sites) and $\{8, 3, 3\}$ ($V_A = 200$ sites) lattice, respectively, are chosen to compute the EE on $\{8, 3, n\}$ lattices with $n = 3, 4, 5, 6$. Notably, the $\{8, 3, 3\}$ subsystem is not computed on the $\{8, 3, 3\}$ lattice itself. The gray dashed lines represent $\pm 5\%$ intervals of the EE computed on the $\{8, 3, 6\}$ lattice. From these results, we observe that by minimizing the boundary effects through enlarging the lattice, we obtain a linear fit of the EE for subsystems in the bulk. Through the finite-size scaling analysis, we show that the boundary effect is considerably excluded to obtain the EE for subsystems in the bulk of the hyperbolic lattice.

APPENDIX E: NUMERICAL ANALYSIS OF SUPER-AREA-LAW SCALING

In this Appendix, we present the numerical analysis to show that the EE does not scale as super-area-law scaling.

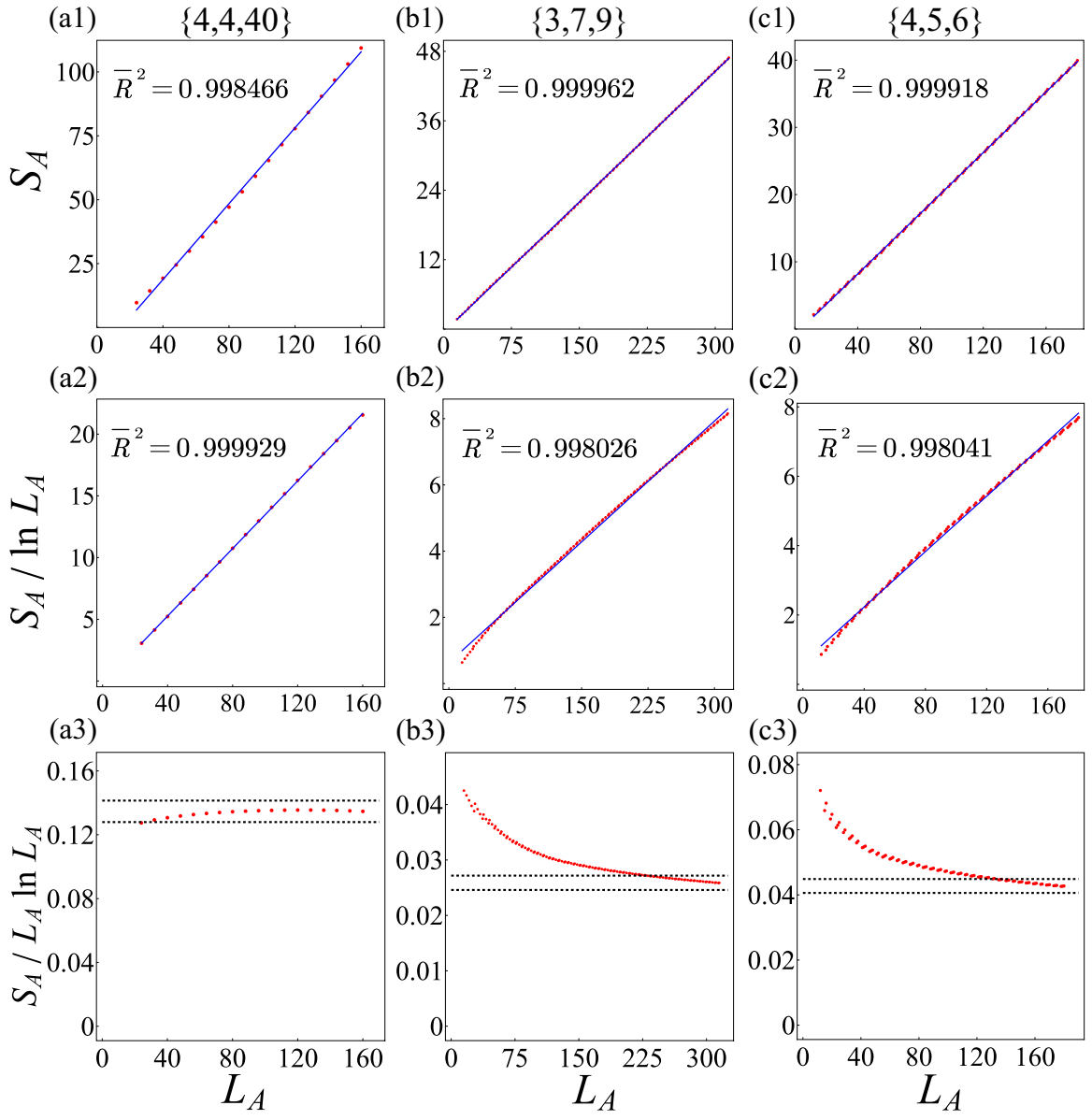

FIG. 12. Columns (a)–(c) correspond to the EE data of {4, 4, 40}, {3, 7, 9}, and {4, 5, 6} shown in Fig. 4. In the top two rows, we present the linear fits $S_A = a_1 L_A + b_1$ and $S_A/\ln L_A = a_2 L_A + b_2$, along with the adjusted coefficient of determination, $\bar{R}^2$. The blue lines represent the respective linear fit functions. In the bottom row, we plot $S_A/L_A \ln L_A$ as a function of L_A, where the dashed lines represent $\pm 5\%$ intervals of the data point corresponding to the biggest L_A.

Specifically, we take the EE data for the gapless free fermions with finite DOS presented in Fig. 4, Sec. III B, as an example. We anticipate the scaling functions $S_A = a_1 L_A + b_1$ and $S_A/\ln L_A = a_2 L_A + b_2$ and fit the EE data. As logarithms can be hard to detect, we select several dimensionless evaluation metrics to compare these two fits, including the adjusted coefficient of determination, $\bar{R}^2$, mean absolute percentage error (MAPE) given by $\frac{100\%}{N}\sum_i^N |\frac{\hat{y}_i - y_i}{y_i}|$, and relative absolute error (RAE) given by $\frac{\sum_i^N |y_i - \hat{y}_i|}{\sum_i^N |y_i - \bar{y}|}$. Here, N is the total number of data points, y_i denotes the true values, $\bar{y}$ denotes the mean of y, and $\hat{y}_i$ denotes the predicted values. A higher $\bar{R}^2$ approaching 1 and lower error estimations approaching 0 indicate a better fitting. The results of these evaluations are listed in Table III, where one can find that area-law fitting is better in the hyperbolic case. We also visualize the fittings in the top two rows of Fig. 12. In the bottom row, we plot $S_A/L_A \ln L_A$ as a function of L_A which only converge in the Euclidean case. Therefore, we conclude that the EE does not scale as a super-area law.

APPENDIX F: ASYMPTOTIC BEHAVIOR OF SCALING COEFFICIENT OF AREA LAW

In this Appendix, we study how the EE varies with q when p is fixed. The number of nearest-neighboring sites of a given site on a hyperbolic lattice, labeled as q as aforementioned, can successively increase. From our findings in the main text,

TABLE III. Results of the adjusted coefficient of determination, $\bar{R}^2$, and dimensionless error estimations, including the mean absolute percentage error (MAPE) and relative absolute error (RAE) for the EE data shown in Fig. 4. In the Euclidean case, the super-area law $S_A/\ln L_A = a_2 L_A + b_2$ is better fit, while in the hyperbolic case, the area law $S_A = a_1 L_A + b_1$ is better.

Lattice	Fit function	$\bar{R}^2$	MAPE (%)	RAE
{4, 4, 40}	area	0.998466	3.66006	3.69134×10^{-2}
	super-area	0.999929	0.338284	7.64020×10^{-3}
{3, 7, 9}	area	0.999962	0.495449	5.79884×10^{-3}
	super-area	0.998026	3.12212	4.06104×10^{-2}
{4, 5, 6}	area	0.999918	0.832573	8.48647×10^{-3}
	super-area	0.998041	2.55588	4.20934×10^{-2}

the EE is proportional to the boundary of subsystem L_A, which is a function of q, and thus the area-law scaling coefficient a should also be related to q. We study the EE for Hamiltonian H_1 on $p = 3, 4, 5$, and 6 hyperbolic lattices with successively increased q and the results are shown in Fig. 13. The results all indicate that as the number of adjacent sites per site q increases, the coefficient a decreases.

Due to computational difficulties on hyperbolic lattices, such as the exponentially growing lattice size and finite-size effect, it is hard to perform the scaling analysis for a lattice with larger q. However, our results here indicate a monotonically decreasing relationship between q and a. It makes sense to explore the relationship of a as q increases, as this may reveal the asymptotic behavior of the EE and provide us with new insights into the hyperbolic geometry.

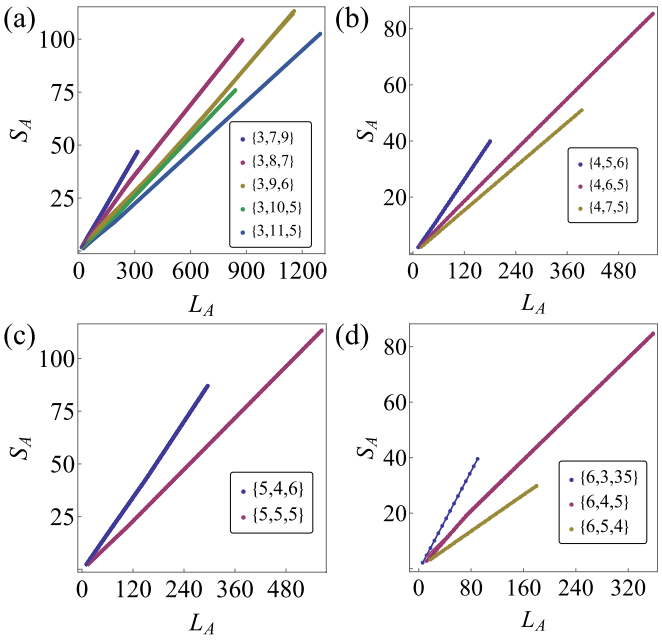

FIG. 13. Asymptotic behavior of coefficient a. The cases for $p = 3, 4, 5$, and 6 all indicate that when q increases, a decreases. Results are computed for Hamiltonian H_1 with $t = 1$ and $\mu = 0$.

[1] L. Amico, R. Fazio, A. Osterloh, and V. Vedral, Entanglement in many-body systems, Rev. Mod. Phys. **80**, 517 (2008).

[2] J. Eisert, M. Cramer, and M. B. Plenio, Colloquium: Area laws for the entanglement entropy, Rev. Mod. Phys. **82**, 277 (2010).

[3] N. Laflorencie, Quantum entanglement in condensed matter systems, Phys. Rep. **646**, 1 (2016).

[4] P. Calabrese and J. Cardy, Entanglement entropy and quantum field theory, J. Stat. Mech. (2004) P06002.

[5] D. A. Abanin, E. Altman, I. Bloch, and M. Serbyn, Colloquium: Many-body localization, thermalization, and entanglement, Rev. Mod. Phys. **91**, 021001 (2019).

[6] W. Li, L. Ding, R. Yu, T. Roscilde, and S. Haas, Scaling behavior of entanglement in two- and three-dimensional free-fermion systems, Phys. Rev. B **74**, 073103 (2006).

[7] T. Barthel, M.-C. Chung, and U. Schollwöck, Entanglement scaling in critical two-dimensional fermionic and bosonic systems, Phys. Rev. A **74**, 022329 (2006).

[8] Y. Zhou and P. Ye, Entanglement signature of hinge arcs, Fermi arcs, and crystalline symmetry protection in higher-order Weyl semimetals, Phys. Rev. B **107**, 085108 (2023).

[9] C. Holzhey, F. Larsen, and F. Wilczek, Geometric and renormalized entropy in conformal field theory, Nucl. Phys. B **424**, 443 (1994).

[10] P. Calabrese and J. Cardy, Entanglement entropy and conformal field theory, J. Phys. A: Math. Theor. **42**, 504005 (2009).

[11] H. Widom, On a class of integral operators with discontinuous symbol, in *Operator Theory: Advances and Applications*, edited by I. Gohbert, Toeplitz Centennila Vol. 4 (Birkhäuser, Basel, 1982), pp. 477–500.

[12] D. Gioev and I. Klich, Entanglement entropy of fermions in any dimension and the Widom conjecture, Phys. Rev. Lett. **96**, 100503 (2006).

[13] H. Leschke, A. V. Sobolev, and W. Spitzer, Scaling of Rényi entanglement entropies of the free Fermi-gas ground state: A rigorous proof, Phys. Rev. Lett. **112**, 160403 (2014).

[14] B. Swingle, Entanglement entropy and the Fermi surface, Phys. Rev. Lett. **105**, 050502 (2010).

[15] Y. Zhou and P. Ye, Entanglement fractalization, Phys. Rev. Res. **6**, 043145 (2024).

[16] W. Magnus, *Noneuclidean Tesselations and Their Groups*, Pure and Applied Mathematics Vol. 61 (Academic Press, New York, 1974).

[17] E. Witten, Anti-de Sitter space and holography, Adv. Theor. Math. Phys. **2**, 253 (1998).

[18] S. Gubser, I. Klebanov, and A. Polyakov, Gauge theory correlators from noncritical string theory, Phys. Lett. B **428**, 105 (1998).

[19] S. Ryu and T. Takayanagi, Holographic derivation of entanglement entropy from the anti–de Sitter space/conformal field theory correspondence, Phys. Rev. Lett. **96**, 181602 (2006).

[20] J. Maldacena, The large N limit of superconformal field theories and supergravity, Adv. Theor. Math. Phys. **2**, 231 (1998).

[21] W. Mück and K. S. Viswanathan, Conformal field theory correlators from classical scalar field theory on anti–de Sitter space, Phys. Rev. D **58**, 041901(R) (1998).

[22] W. Mück and K. S. Viswanathan, Conformal field theory correlators from classical field theory on anti–de Sitter space: Vector and spinor fields, Phys. Rev. D **58**, 106006 (1998).

[23] M. Henningson and K. Sfetsos, Spinors and the AdS/CFT correspondence, Phys. Lett. B **431**, 63 (1998).

[24] T. Nishioka, Entanglement entropy: Holography and renormalization group, Rev. Mod. Phys. **90**, 035007 (2018).

[25] J. I. Cirac, D. Pérez-García, N. Schuch, and F. Verstraete, Matrix product states and projected entangled pair states: Concepts, symmetries, theorems, Rev. Mod. Phys. **93**, 045003 (2021).

[26] R. C. Brower, C. V. Cogburn, A. L. Fitzpatrick, D. Howarth, and C.-I. Tan, Lattice setup for quantum field theory in AdS_2, Phys. Rev. D **103**, 094507 (2021).

[27] M. Asaduzzaman, S. Catterall, J. Hubisz, R. Nelson, and J. Unmuth-Yockey, Holography on tessellations of hyperbolic space, Phys. Rev. D **102**, 034511 (2020).

[28] R. C. Brower, C. V. Cogburn, and E. Owen, Hyperbolic lattice for scalar field theory in AdS_3, Phys. Rev. D **105**, 114503 (2022).

[29] S. Dey, A. Chen, P. Basteiro, A. Fritzsche, M. Greiter, M. Kaminski, P. M. Lenggenhager, R. Meyer, R. Sorbello, A. Stegmaier, R. Thomale, J. Erdmenger, and I. Boettcher, Simulating holographic conformal field theories on hyperbolic lattices, Phys. Rev. Lett. **133**, 061603 (2024).

[30] A. J. Kollár, M. Fitzpatrick, and A. A. Houck, Hyperbolic lattices in circuit quantum electrodynamics, Nature (London) **571**, 45 (2019).

[31] S. Yu, X. Piao, and N. Park, Topological hyperbolic lattices, Phys. Rev. Lett. **125**, 053901 (2020).

[32] W. Zhang, H. Yuan, N. Sun, H. Sun, and X. Zhang, Observation of novel topological states in hyperbolic lattices, Nat. Commun. **13**, 2937 (2022).

[33] P. M. Lenggenhager, A. Stegmaier, L. K. Upreti, T. Hofmann, T. Helbig, A. Vollhardt, M. Greiter, C. H. Lee, S. Imhof, H. Brand, T. Kießling, I. Boettcher, T. Neupert, R. Thomale, and T. Bzdušek, Simulating hyperbolic space on a circuit board, Nat. Commun. **13**, 4373 (2022).

[34] J. Chen, F. Chen, L. Yang, Y. Yang, Z. Chen, Y. Wu, Y. Meng, B. Yan, X. Xi, Z. Zhu, M. Cheng, G.-G. Liu, P. P. Shum, H. Chen, R.-G. Cai, R.-Q. Yang, Y. Yang, and Z. Gao, AdS/CFT Correspondence in hyperbolic lattices, arXiv:2305.04862.

[35] L. Huang, L. He, W. Zhang, H. Zhang, D. Liu, X. Feng, F. Liu, K. Cui, Y. Huang, W. Zhang, and X. Zhang, Hyperbolic photonic topological insulators, Nat. Commun. **15**, 1647 (2024).

[36] A. Gendiar, Area-law study of quantum spin system on hyperbolic lattice geometries, Acta Phys. Pol. A **137**, 589 (2020).

[37] K. Okunishi and T. Nishino, Holographic analysis of boundary correlation functions for the hyperbolic-lattice Ising model, Prog. Theor. Expt. Phys. (2024) 093A02.

[38] D. Saraidaris and A. Jahn, Critical spin models from holographic disorder, arXiv:2409.17235.

[39] X. Zhu, J. Guo, N. P. Breuckmann, H. Guo, and S. Feng, Quantum phase transitions of interacting bosons on hyperbolic lattices, J. Phys.: Condens. Matter **33**, 335602 (2021).

[40] I. Boettcher, P. Bienias, R. Belyansky, A. J. Kollár, and A. V. Gorshkov, Quantum simulation of hyperbolic space with circuit quantum electrodynamics: From graphs to geometry, Phys. Rev. A **102**, 032208 (2020).

[41] T. Tummuru, A. Chen, P. M. Lenggenhager, T. Neupert, J. Maciejko, and T. Bzdušek, Hyperbolic non-Abelian semimetal, Phys. Rev. Lett. **132**, 206601 (2024).

[42] A. Chen, J. Maciejko, and I. Boettcher, Anderson localization transition in disordered hyperbolic lattices, Phys. Rev. Lett. **133**, 066101 (2024).

[43] Z.-R. Liu, C.-B. Hua, T. Peng, and B. Zhou, Chern insulator in a hyperbolic lattice, Phys. Rev. B **105**, 245301 (2022).

[44] D. M. Urwyler, P. M. Lenggenhager, I. Boettcher, R. Thomale, T. Neupert, and T. Bzdušek, Hyperbolic topological band insulators, Phys. Rev. Lett. **129**, 246402 (2022).

[45] Z.-R. Liu, C.-B. Hua, T. Peng, R. Chen, and B. Zhou, Higher-order topological insulators in hyperbolic lattices, Phys. Rev. B **107**, 125302 (2023).

[46] Y.-L. Tao and Y. Xu, Higher-order topological hyperbolic lattices, Phys. Rev. B **107**, 184201 (2023).

[47] N. Gluscevich, A. Samanta, S. Manna, and B. Roy, Dynamic mass generation on two-dimensional electronic hyperbolic lattices, Phys. Rev. B **111**, L121108 (2025).

[48] A. Chen, Y. Guan, P. M. Lenggenhager, J. Maciejko, I. Boettcher, and T. Bzdušek, Symmetry and topology of hyperbolic Haldane models, Phys. Rev. B **108**, 085114 (2023).

[49] F. R. Lux and E. Prodan, Converging periodic boundary conditions and detection of topological gaps on regular hyperbolic tessellations, Phys. Rev. Lett. **131**, 176603 (2023).

[50] C. Sun, A. Chen, T. Bzdušek, and J. Maciejko, Topological linear response of hyperbolic Chern insulators, SciPost Phys. **17**, 124 (2024).

[51] P. M. Lenggenhager, S. Dey, T. Bzdušek, and J. Maciejko, Hyperbolic spin liquids, arXiv:2407.09601.

[52] F. Dusel, T. Hofmann, A. Maity, Y. Iqbal, M. Greiter, and R. Thomale, Chiral gapless spin liquid in hyperbolic space, arXiv:2407.15705.

[53] A.-L. He, L. Qi, Y. Liu, and Y.-F. Wang, Hyperbolic fractional Chern insulators, Phys. Rev. B **110**, 195113 (2024).

[54] I. Boettcher, A. V. Gorshkov, A. J. Kollár, J. Maciejko, S. Rayan, and R. Thomale, Crystallography of hyperbolic lattices, Phys. Rev. B **105**, 125118 (2022).

[55] J. Maciejko and S. Rayan, Hyperbolic band theory, Sci. Adv. **7**, eabe9170 (2021).

[56] J. Maciejko and S. Rayan, Automorphic Bloch theorems for hyperbolic lattices, Proc. Natl. Acad. Sci. USA **119**, e2116869119 (2022).

[57] P. M. Lenggenhager, J. Maciejko, and T. Bzdušek, Non-Abelian hyperbolic band theory from supercells, Phys. Rev. Lett. **131**, 226401 (2023).

[58] N. Cheng, F. Serafin, J. McInerney, Z. Rocklin, K. Sun, and X. Mao, Band theory and boundary modes of high-dimensional representations of infinite hyperbolic lattices, Phys. Rev. Lett. **129**, 088002 (2022).

[59] G. Shankar and J. Maciejko, Hyperbolic lattices and two-dimensional Yang-Mills theory, Phys. Rev. Lett. **133**, 146601 (2024).

[60] L. Boyle, M. Dickens, and F. Flicker, Conformal quasicrystals and holography, Phys. Rev. X **10**, 011009 (2020).

[61] A. Jahn, Z. Zimborás, and J. Eisert, Central charges of aperiodic holographic tensor-network models, Phys. Rev. A **102**, 042407 (2020).

[62] R. Mosseri and J. Vidal, Density of states of tight-binding models in the hyperbolic plane, Phys. Rev. B **108**, 035154 (2023).

[63] R. Haydock, V. Heine, and M. J. Kelly, Electronic structure based on the local atomic environment for tight-binding bands, J. Phys. C **5**, 2845 (1972).

[64] R. Haydock and M. Kelly, Surface densities of states in the tight-binding approximation, Surf. Sci. **38**, 139 (1973).

[65] R. Haydock, V. Heine, and M. J. Kelly, Electronic structure based on the local atomic environment for tight-binding bands. II, J. Phys. C **8**, 2591 (1975).

[66] Z.-K. Lin, Y. Zhou, B. Jiang, B.-Q. Wu, L.-M. Chen, X.-Y. Liu, L.-W. Wang, P. Ye, and J.-H. Jiang, Measuring entanglement entropy and its topological signature for phononic systems, Nat. Commun. **15**, 1601 (2024).

[67] R. Orús, A practical introduction to tensor networks: Matrix product states and projected entangled pair states, Ann. Phys. **349**, 117 (2014).

[68] T. Xiang, *Density Matrix and Tensor Network Renormalization* (Cambridge University Press, Cambridge, 2023).

[69] H. Li and F. D. M. Haldane, Entanglement spectrum as a generalization of entanglement entropy: Identification of topological order in non-Abelian fractional quantum Hall effect states, Phys. Rev. Lett. **101**, 010504 (2008).

[70] L. Fidkowski, Entanglement spectrum of topological insulators and superconductors, Phys. Rev. Lett. **104**, 130502 (2010).

[71] C. H. Lee, P. Ye, and X.-L. Qi, Position-momentum duality in the entanglement spectrum of free fermions, J. Stat. Mech. (2014) P10023.

[72] I. Klich, Lower entropy bounds and particle number fluctuations in a Fermi sea, J. Phys. A: Math. Gen. **39**, L85 (2006).

[73] I. Peschel, Calculation of reduced density matrices from correlation functions, J. Phys. A: Math. Gen. **36**, L205 (2003).

[74] C. H. Lee and P. Ye, Free-fermion entanglement spectrum through Wannier interpolation, Phys. Rev. B **91**, 085119 (2015).

[75] H.-H. Lai and K. Yang, Entanglement entropy scaling laws and eigenstate typicality in free fermion systems, Phys. Rev. B **91**, 081110(R) (2015).

[76] N. Crampé, R. I. Nepomechie, and L. Vinet, Free-fermion entanglement and orthogonal polynomials, J. Stat. Mech. (2019) 093101.

[77] L.-M. Chen, S. A. Chen, and P. Ye, Entanglement, non-Hermiticity, and duality, SciPost Phys. **11**, 003 (2021).

[78] C. H. Lee, Exceptional bound states and negative entanglement entropy, Phys. Rev. Lett. **128**, 010402 (2022).

[79] G. C. Levine and D. J. Miller, Zero-dimensional area law in a gapless fermionic system, Phys. Rev. B **77**, 205119 (2008).

[80] L. Ding, N. Bray-Ali, R. Yu, and S. Haas, Subarea law of entanglement in nodal fermionic systems, Phys. Rev. Lett. **100**, 215701 (2008).

[81] M. B. Hastings, An area law for one-dimensional quantum systems, J. Stat. Mech. (2007) P08024.

[82] L. Herviou, N. Regnault, and J. H. Bardarson, Entanglement spectrum and symmetries in non-Hermitian fermionic noninteracting models, SciPost Phys. **7**, 069 (2019).

[83] P.-Y. Chang, J.-S. You, X. Wen, and S. Ryu, Entanglement spectrum and entropy in topological non-Hermitian systems and nonunitary conformal field theory, Phys. Rev. Res. **2**, 033069 (2020).

[84] R. Modak and B. P. Mandal, Eigenstate entanglement entropy in a $\mathcal{PT}$-invariant non-Hermitian system, Phys. Rev. A **103**, 062416 (2021).

[85] Y.-B. Guo, Y.-C. Yu, R.-Z. Huang, L.-P. Yang, R.-Z. Chi, H.-J. Liao, and T. Xiang, Entanglement entropy of non-Hermitian free fermions, J. Phys.: Condens. Matter **33**, 475502 (2021).

[86] Y.-T. Tu, Y.-C. Tzeng, and P.-Y. Chang, Rényi entropies and negative central charges in non-Hermitian quantum systems, SciPost Phys. **12**, 194 (2022).

[87] C. Ortega-Taberner, L. Rødland, and M. Hermanns, Polarization and entanglement spectrum in non-Hermitian systems, Phys. Rev. B **105**, 075103 (2022).

[88] L.-M. Chen, Y. Zhou, S. A. Chen, and P. Ye, Quantum entanglement of non-Hermitian quasicrystals, Phys. Rev. B **105**, L121115 (2022).

[89] K. Kawabata, T. Numasawa, and S. Ryu, Entanglement phase transition induced by the non-Hermitian skin effect, Phys. Rev. X **13**, 021007 (2023).

[90] Y.-Y. Zou, Y. Zhou, L.-M. Chen, and P. Ye, Detecting bulk and edge exceptional points in non-Hermitian systems through generalized Petermann factors, Front. Phys. **19**, 23201 (2023).

[91] Y. L. Gal, X. Turkeshi, and M. Schirò, Volume-to-area law entanglement transition in a non-Hermitian free fermionic chain, SciPost Phys. **14**, 138 (2023).

[92] C.-T. Hsieh and P.-Y. Chang, Relating non-Hermitian and Hermitian quantum systems at criticality, SciPost Phys. Core **6**, 062 (2023).

[93] W.-Z. Yi, Y.-J. Hai, R. Xiao, and W.-Q. Chen, Exceptional entanglement in non-Hermitian fermionic models, arXiv:2304.08609.

[94] L. Zhou, Entanglement phase transitions in non-Hermitian quasicrystals, Phys. Rev. B **109**, 024204 (2024).

[95] S.-Z. Li, X.-J. Yu, and Z. Li, Emergent entanglement phase transitions in non-Hermitian Aubry-André-Harper chains, Phys. Rev. B **109**, 024306 (2024).

[96] L. Zhou, Entanglement phase transitions in non-Hermitian Floquet systems, Phys. Rev. Res. **6**, 023081 (2024).

[97] W.-T. Xue and C. H. Lee, Topologically protected negative entanglement, arXiv:2403.03259.

[98] S. Shi, L. Dong, J. Bao, and B. Guo, Entanglement entropy and topological properties in a long-range non-Hermitian Su-Schrieffer-Heeger model, Phys. B: Condens. Matter **674**, 415601 (2024).

[99] D. F. Munoz-Arboleda, R. Arouca, and C. Morais Smith, Thermodynamics and entanglement entropy of the non-Hermitian SSH model, Phys. Rev. B **110**, 115135 (2024).

[100] Z. Yang, C. Lu, and X. Lu, Entangelment entropy on generalized Brillouin zone, Phys. Rev. B **110**, 235127 (2024).

[101] J. P. Gaspard and F. Cyrot-Lackmann, Density of states from moments. Application to the impurity band, J. Phys. C **6**, 3077 (1973).

[102] R. Haydock and C. M. M. Nex, Comparison of quadrature and termination for estimating the density of states within the recursion method, J. Phys. C **17**, 4783 (1984).